NTNU – Trondheim
Norwegian University of
Science and Technology

Mapping Orientation Distribution of Talc Particles in Polypropylene by Small-Angle X-ray Scattering Tomography

Eirik Torbjørn Bakken
Skjønsfjell

Master of Science in Physics and Mathematics
Submission date: September 2013
Supervisor: Dag Werner Breiby, IFY

Norwegian University of Science and Technology
Department of Physics

Abstract

Small-angle X-ray scattering tomography has for the first time been used to investigate the spatially resolved orientation distribution of talc particles in a sample of injection molded isotactic polypropylene, where the particles had a preferred orientation along the axis of the injection. The scattering patterns in the direction perpendicular to the rotation axis of the tomography scan were used to retrieve the orientation distribution in a 2D cross section of the sample.

Two different methods are presented, one using a numerical approach of Simulated Annealing and one method using a linear set of equations to find the distances the X-ray beam travels through the different orientation regions. The method of Simulated Annealing showed little to no promise in retrieving the orientation distribution while the method using a linear set of equations is successful at retrieving the main features of the orientation distribution. The resolution is however not yet good enough to distinguish fine details inside the sample.

It is believed that with further work on the model used and additional constraints on the reconstruction algorithm higher precision in the retrieved orientation distribution can be achieved.

Sammendrag

Småvinkelrøntgenspredningtomografi (SAXS tomography) har for første gang blitt benyttet for å undersøke retningsdistribusjonen av talkpartikler i en prøve av injeksjonssprøytet isotaktisk polypropylen, hvor talkpartiklene hadde en preferert retning langs injeksjonsaksen. Spredningssignalene i retningen normalt på rotasjonsaksen i tomografiskannet ble benyttet til å ekstrahere retningsdistribusjonen i et 2D tversnitt av prøven.

To forskjellige metoder er presentert, én benytter seg av den numeriske metoden simulert avspenning (Simulated Annealing), og én metode benytter seg av et lineært set av likninger for å finne avstandene røntgenstrålen går gjennom de forskjellige regionene med forskjellig orientering. Metoden som benyttet simulert avspenning viste lite til ikke noe håp om å gjenskape retningsdistribusjonen, mens metoden som benyttet et lineært sett av likninger er vellykket i å rekonstruere de karakteristiske kjennemerkene av retningsdistribusjonen. Oppløsningen er derimot ikke god nok til å separere detaljer inne i prøven.

Det er tro på at det vil være mulig å øke presisjonen i å gjenfinne retningsdistribusjonen ved å jobbe videre på rekonstruksjonsalgoritmen og tillegge flere føringer.

Preface

This thesis is the final part of a masters degree in Applied Physics at the Norwegian University of Science and Technology (NTNU). The degree is estimated to take five years, and include a minimum of 300 credits. 30 of these credits are from this thesis and is normally written the very last semester of the education. Due to an internship i Germany my last semester was shifted a few months and this thesis was written in the period April-September 2013, a little later than normal. This thesis is in the field of condensed matter physics and X-ray imaging and investigates how X-rays can be applied to imaging materials.

I would like to thank PhD. students Håvard Granlund and Jostein Bø Fløystad in the X-ray group at NTNU for truly invaluable help. A very special thanks also to my supervisor, Dag W. Breiby, Associate professor at the Department of Physics, for continuous support and guidance in finalizing this project. Without discussing and reformulating the problems which arose during this thesis it would not be possible to get as far in the project as I did.

The work done in this project is based both on real life experiments and on computer simulations. The real life experiments were performed at the Swiss Light Source (SLS) in November 2012, by PhD. student Håvard Granlund, associate professor Dag W. Breiby and post doc. Kristin Høydalsvik, along with the scientific staff at the cSAXS beamline. I would send a great thank to those who performed the experiment for letting me work with the data. A thank also to SINTEF for supplying the sample used.

Since it is very little literature regarding SAXS-tomography I had no template for what to do in this thesis. The method presented in this thesis is an idea by myself and a first step towards using the entire SAXS-signal in computed tomography. I hope to continue on this project later and make it good enough to make use of it for different kind of samples.

Contents

List of Figures

Chapter 1

Introduction

1.1 Background for Project

This project has focused on Small-Angle X-ray Scattering (SAXS) tomography of talc filled isotactic polypropylene (iPP). This means that an iPP sample has been illuminated by X-rays, and the scattered rays at small angles have been recorded and analyzed. The goal was to get three-dimensional orientation distribution of the talc particles inside the polypropylene by the use of computed tomography.

1.2 Computational Tomography

Computed Tomography (CT) was developed in the late 70's, and Allan M. Cormack and Godfrey N. Hounsfield were awarded the Nobel prize in medicine in 1979 for the development of CT[1]. Since that time tomography has been well known in the medical and scientific community, and many people are familiar with the images a hospital CT-scanner acquires. In short, tomography consists of a series of line scans of a sample. The sample is rotated between each line scan and this is done until the sample has been rotated 180 degrees. The projections are then used to recreate the sample imaged. Ordinary tomography done in a hospital is usually based on imaging the attenuation coefficients of a cross section of a patient. This makes it possible for a doctor to view different organs or tumors, because various components inside the body attenuates X-rays differently, and will therefore have different attenuation coefficients. The method of attenuation-based imaging of various objects with the use of computational tomography is rather well

---

[1] as listed at www.nobelprize.org

explored by Kak and Slaney [1]. In recent years the development in X-ray physics, better synchrotron sources with higher brilliance and coherence than before, and high resolution detectors with high signal to noise ratio and fast read out time has made it possible to do tomography based on the *scattered* X-ray signal. This can be done with both the wide-angle signal, or the small-angle signal, depending on what information one is looking for.

1.3 SAXS Tomography

Earlier work in SAXS tomography has only looked at the scattering in the direction along the rotation axis, or assumed that the scattering particles are spherically symmetric [2, 3, 4]. With these constraints or assumptions there are very few systems which can be imaged, or it is possible to only get information of the scattering cross section in the direction along the rotation axis. No method exists for making use of the scattering in the direction perpendicular to the rotation axis. This is due to the fact that the assumptions ordinary tomographic reconstruction techniques are based on are invalid when the scattering perpendicular to the rotation axis is used in a direct way, by for example just putting in the recorded intensity in to the reconstruction algorithm.

1.4 Objective for Thesis

The project this thesis is based on is trying to use the scattering in the direction perpendicular to the rotation axis, hereafter called horizontal scattering, to get information on how the talc particles are oriented inside a piece of isotactic polypropylene. The goal was not to discover the orientation of the talc particles, but to see if, and how well, the 3D orientation distribution could be retrieved by SAXS tomography. Earlier work had already mapped the orientation distribution of the talc particles in the same kind of sample [5] and served as reference to see if the method would work.

The techniques explored in this thesis would of course not only be relevant for talc particles in polypropylene, but for all kind of different particles, as long as the scattering particles mostly are of the same material and same shape. Discovering a technique which can give the 3 dimensional orientation of particles inside a sample would be very interesting for both industry and science. Tiny particles can affect many meso- and macroscopical properties like structural integrity of a sample or the index of refraction. Particles with biaxial index of refraction have different dielectric constants in different directions and will therefore have different optical properties depending on how they are oriented. There are many more examples of *anisotropic* microparticles, i. e., particles that have different properties in different directions of their shape. By developing a tomographic technique to see how they are oriented inside a sample, it is possible to predict the sample's properties or modify the manufacturing method to get the desired orientation distribution. To get the full orientation distribution of micro particles the sample would normally have to be cut open to get a measurement of the cross section. Retrieving the orientation distribution without destroying the sample itself can truly be invaluable. Cutting the sample could perhaps also alter the orientation of the particles at the surface because the cutting blade can move particles around, giving erroneous results when doing measurements. In addition, physically altering the sample will make it useless for many further studies. By mapping the 3D orientation distribution without destroying the sample, it will be possible to do *in situ* studies of material reorganization during mechanical loading. This can give predictions on which parts in the sample will break first, during for instance a stress test.

Other methods for doing *in situ* studies of materials exist, as for instance *ptychography* [6]. This method is a version of coherent diffraction imaging and is imaging based on the real part of the index of refraction. It is possible to do tomography with this technique, and the resolution can be as good as < 100 nm. The problem is that this method is not suited to handle as large objects as the sample investigated in this thesis. In ptychography an X-ray beam is raster scanned across the sample. The beam spot of each scan has to partly overlap the previous beam spot in order for the constraints of the reconstruction algorithm to work. The time to investigate an entire sample would therefore be too long. It is also possible to imagine conventional absorption tomography to be used in mapping the orientation distribution of the talc particles in the sample. The attenuation coefficient of talc and polypropylene should have good contrast. It will however not be possible, since the particles are smaller than the beam, thus not making it possible to distinguish talc and polypropylene.

1.5 Structure of Thesis

This thesis will start with a short description of the materials used in the experiment, and why they are suited for this project. The report will then continue with a theory section, explaining how scattering occurs and what it is that influences the small-angle scattering signal. Computational tomography will also be presented, with a section on why general reconstruction algorithms do not work for the horizontal scattering. After this follows an experimental part explaining how the practical experiment was performed, and how the computer simulations and reconstructions were set up. Then the results will be presented and discussed, before the conclusion of the project will be drawn.

Chapter 2

The Sample Analyzed

2.1 The Experimental Sample

The sample used in the experimental part of this thesis was delivered by SINTEF and was a piece of injection molded talc filled isotactic polypropylene. The shape of the sample resembled a dog bone, and can be seen in Figure 2.1. The experiment itself was performed at the middle of the dog bone neck with the axis of rotation parallel to the injection flow of the polymer. The sample provided was part of a series of injection molded samples manufactured under different conditions. Each sample had a designation *EDXY*. The two first letters, *ED*, represents the material, while the two last letters represents the manufacturing parameters. The third letter, *X*, is referring to the mold temperature and is either *L* (low temperature), *M* (medium temperature) or *H* (high temperature). The last letter, *Y*, refers to the shear rate during production of the sample. The shear rate is either *L* (low), *M* (medium) or *H* (high). A sample made under medium temperature and high shear rate would for example have designation *EDMH* . The values for the low, medium and high temperature and shear rate are given in table 2.1.

When neglecting the solidifying layer at the walls the shear rate, $\dot{\gamma}$, is given by [7]

$$\dot{\gamma} = 3\frac{Q}{Ah}. \tag{2.1}$$

Q is the volumetric flow rate in m^3/s, A is the area of the cross section of the mold and h is the smallest dimension of the cross section. The shear rate governs the injection speed of the melt and the pressure applied during solidification [7].

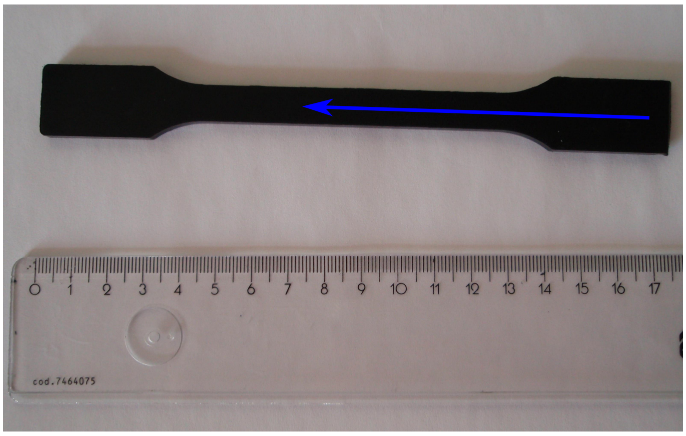

Figure 2.1: Image of the polypropylene sample used in the experiment. The shape resembles a dog-bone and the ruler gives the dimensions in cm and the blue arrow indicates the direction the melted polypropylene flowed in to the mold.

Table 2.1: The values for low, medium and high temperature and shear rate during the manufacturing of the samples.

	Shear rate s^{-1}	Temperature °C
Low	25	20
Medium	150	40
High	850	65

For this particular project, only a sample made by injection molding under low temperature and low shear rate was used. It will thus not be any comparison between samples constructed under different conditions. It is still chosen to present this representation of the other samples to make it easier to compare the results and samples with earlier work performed at the X-ray group at NTNU [7, 8] and possible later work with the same kind of samples constructed under different conditions.

This sample was well suited for this project because talc particles and polypropylene give a strong signal due to the large contrast between in the scattering length density. The talc particles also had a preferred direction, thus making the problem less complex because less variables were unknown.

2.2 Polypropylene

Polypropylene, also referred to as polypropene, is a common polymer used in a large variety of items. The isotactic variant of polypropylene was first created by Natta and Rehn in 1954 [9] and is now one of the most important "plastics" in the world, with an estimated worldwide generated revenue of more than US $145 billion in the year 2019 [10]. The average growth the past eight years has been 4.4 % and will likely be surpassed in the coming years [10]. Polypropylene is a material consisting of a repeating cell of propene, as described in Figure 2.2.

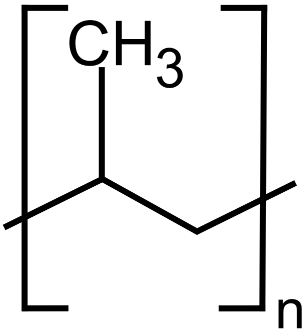

Figure 2.2: The repeating cell of polypropylene. n is a number in the range of ten thousands. A carbon atom with attached hydrogen atoms is placed at each kink of the polymer chain.

The material in this study is of the type *isotactic* polypropylene. This means that the methyl-groups all sit on the "same" side, shown in Figure 2.3 (a), and that the polymer chain is along a straight axis, without sharp bends. Another type of polypropylene is shown in Figure 2.3 (b). This is syndiotactic polypropylene and will not be discussed further, but is shown to emphasize that polypropylene can form different kinds of chains. Whether the polypropylene is isotactic or not has implications on the polymer's ability to form crystals. Polypropylene with lower isotacticity, meaning more defects from a perfect isotactic chain, will form smaller crystals [11].

Isotactic polypropylene crystallizes in four different phases: α (monoclinic), β (hexagonal), γ (triclinic) and smectic, with α usually the dominant phase [12]. The structure of the unit cell in the α form is $a = 0.666$ nm, $b = 2.078$ nm, $c = 0.6495$ nm, $\beta = 99.62°$ and $\alpha = \gamma = 90°$, where the chain is along

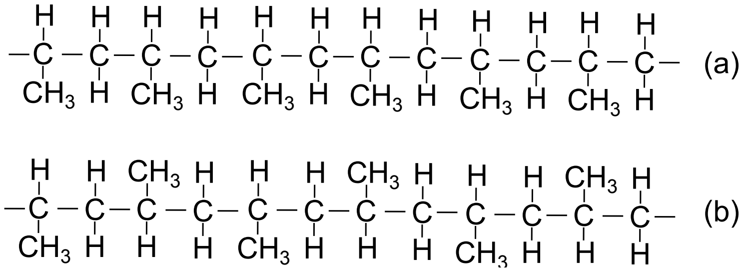

Figure 2.3: (a) shows isotactic polypropylene, while (b) shows syndiotactic polypropylene.

the *c*-axis [13]. Which form the polypropylene crystallizes to depends on factors such as temperature [14] and shear strength [15]. Decreasing tacticity also has the implication of lower melting temperature and that more of the polypropylene will crystallize in the γ-phase [11]. The mass density of polypropylene depends on the degree of crystallinity, but is approximately $\rho = 0.90$ g/cm^3[16], and has attenuation coefficient $\mu = 0.94$ cm^{-1} for X-rays with wavelengths of 1 Å [16].

The polypropylene samples used in this project were injection molded. This is a process where thermoplastics are forced into a heated barrel where it is melted and mixed, typically by a revolving screw inside the barrel. This screw also forces the plastic forward from the intake towards the outlet where the mold is attached. The plastic is then injected to the mold cavity with a lower temperature, which cools and solidifies the plastic almost as soon as the mold is filled. Injection molding is the most used method to produce thermoplastic products [17].

2.3 Talc

Talc is a mineral with chemical formula $H_2Mg_3(SiO_3)_4$ and crystallizes in a monoclinic unit cell with parameters $a = 5.26$ Å, $b = 9.1$ Å, $c = 18.81$ Å and $\beta = 100°$ [5], and has mass density of approximately[1] $\rho = 2.69$ g/cm^3. With these parameters the absorption coefficient of talc can be calculated to be $\mu = 23.1$ cm^{-1} [16] for X-rays with wavelengths 1 Å. Talc gives a number of effects when added to polypropylene. The ability to reinforce polymers [18] is one of the advantages, in addition to reducing shrinkage and warpage, and

---

[1] Chemical tables from various suppliers, found online, list the density of talc in the range of 2.5-2.8 g/cm^3

to reduce thermal expansion and the cycle time [5]. For these reasons talc have been added to the polypropylene samples. Better understanding of how the talc behaves inside the polymer is thus a crucial step to understand the properties of this kind of polypropylene.

It has been shown in earlier studies that the talc particles in the isotactic polyropylene sample form thin flakes, with their surface normal parallel to the sample surface normals both by WAXS and SAXS raster scans of a cross section of the sample [5, 8]. The orientation of the talc flakes is indicated in Figure 2.4. It is clear that the talc particles are orienting themselves with their surface normal perpendicular to the outer surface of the sample, and it is perfect agreement between the WAXS and SAXS measurement.

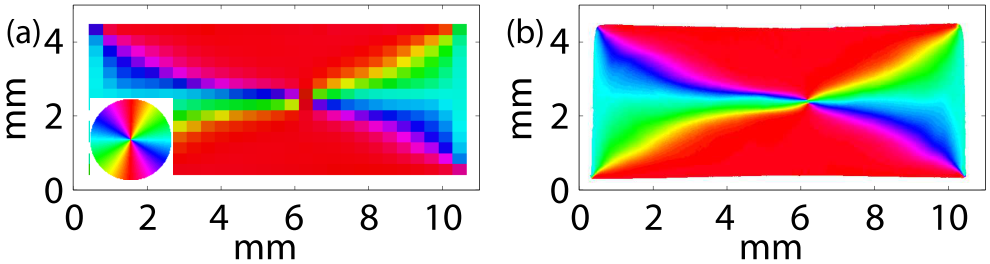

Figure 2.4: Orientation of the talc flakes in the iPP sample from a cross section of the dog bone neck, perpendicular to the flow direction. (a) Is the direction of the talc *c*-axis measured by raster scanning WAXS, while (b) is the direction of the talc flakes surface normal measured by raster scanning SAXS. The direction is given by the color wheel inset. Figures adapted from [8]

The shape and dimension of the talc particles were measured earlier by Scanning Electron Microscopy (SEM) at NTNU NanoLab by Per Erik Vullum representing SINTEF. Two of these measurement are shown in Figure 2.5. Figure 2.5 (a) is shown with 2500x magnification, and is shown to indicate the large spread in size of the particles. Figure 2.5 (b) is shown with 5000x magnification and shows better the size and shape of individual particles. In general, it looks like the diameter of the talc particles varies from 1-10 μm and the height varies from 0.1-2 μm. Because the talc particles are very much polydispersive it can be expected that the scattering signal will be smoothed out, and characteristics features for talc particles with one specific geometry will not be discernible.

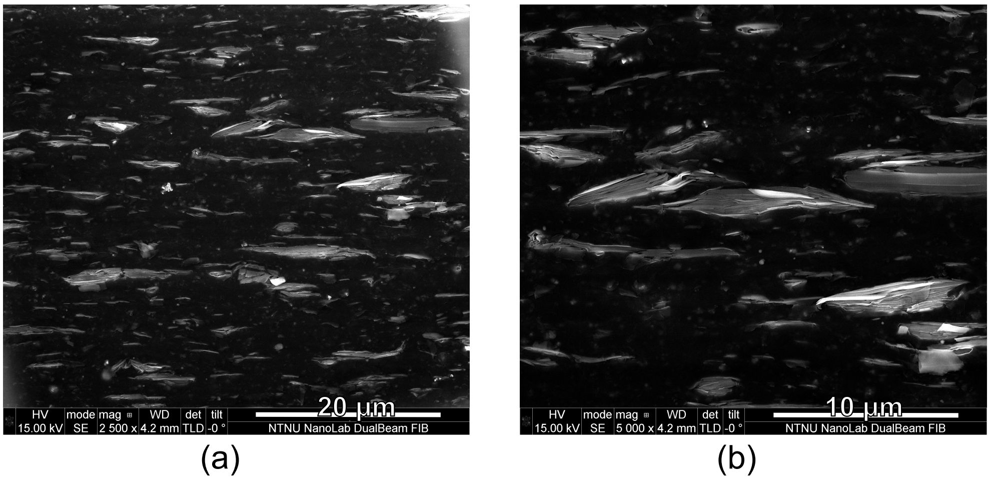

Figure 2.5: The size and shape of the talc particles in the polypropylene sample measured with scanning electron microscopy (SEM). (a) Image taken with 2500x magnification. (b) Image taken with 5000x magnification.

Chapter 3

Theory

3.1 A Brief Note on Notation

In this chapter the theory of what has been done in this thesis will be presented. The main goal has been to retrieve the orientation distribution of talc particles inside a sample of polypropylene. This will lead to a number of different coordinate systems being used to see how the different samples are oriented with respect to each other. To keep notations for these different coordinate systems consistent throughout the thesis some notation can use slightly different symbols than other literature. The notation of the different coordinate systems, and what they are associated with, will be presented in this section. How the three different coordinate systems used are related to each other can be seen in Figure 3.1.

The Cartesian (x, y, z)-coordinate systems refer to the laboratory frame. This is the fixed coordinate system setting the basis for all the angles between the other coordinate systems. The x-component represents the horizontal direction perpendicular to the direction the horizontal X-ray beam travels. The y-component is along the X-ray beam while the z-component is representing the vertical direction perpendicular to the beam as illustrated in Figure 4.2.

The iPP sample itself has a rectangular shape. The coordinate system of the iPP sample is (s, t, z) and is referred to as the sample frame. The s-coordinate is along the long edge of the sample, the t-coordinate is along the short edge of the sample, while the z-component is in the same direction as for the laboratory frame. When the entire sample is rotated with respect to the laboratory frame, the (s, t, z) coordinate system is rotated an equal amount, and the angle between the sample frame s-axis and laboratory frame

x-axis forms an angle ψ.

Each talc particle is also given its own coordinate system, referred to as the talc frame. This Cartesian coordinate system is aligned with the internal symmetry of the talc particles and has components (x', y', z'). How these components are oriented compared to the shape of the talc particle can be seen in Figure 3.2 and 4.4. The different talc particles have various orientation inside the iPP sample. The angle a talc particle has inside the iPP sample has the symbol ϕ, which means that the angle between the s-axis in the sample frame and the x'-axis in the talc frame is ϕ. The angle between the talc frame and laboratory frame is $\xi = \psi + \phi$.

Associated reciprocal coordinate systems are used. To which coordinate system in real space these are related is determined by a subindex. For instance, q_x is the component of the scattering vector in the x-direction of the laboratory frame, while the scattering vector $q_{x'}$ is the scattering vector in the x'-direction of the talc frame.

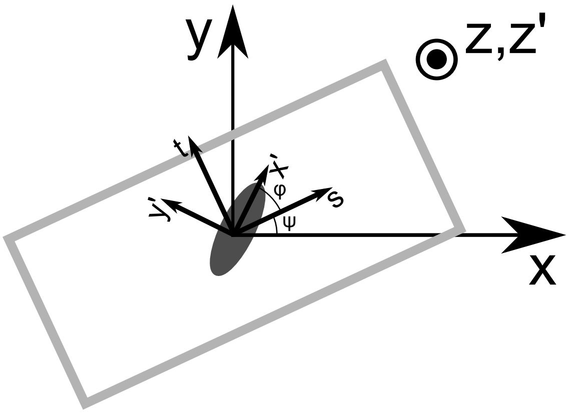

Figure 3.1: The figure shows the three different coordinate systems used, and how they are related. The xy-coordinate system is the fixed laboratory frame. The st-system is the sample frame, and the sample is outlined by the light gray rectangle. The angle between the laboratory frame and the sample frame is ψ about the z-axis. The talc particle is outlined by the dark gray disk, and the talc frame has coordinate system $x'y'$. The angle between the talc frame and the sample frame is ϕ, also all three coordinate systems have their z-axis parallel and out of the paper plane.

3.2 Fundamentals of Electromagnetic Waves

It is normal to make two different descriptions when describing X-rays. Either the classical view is adapted, and an X-ray beam is imagined as a propagating wave in compliance with Maxwell's equations, or an X-ray beam is regarded as a stream of quantified photons. Which description is best depends on which optical phenomenon is considered.

When regarding X-rays as electromagnetic waves, it is normal to adopt the formalism of describing the electric part of the wave with complex numbers

$$\mathbf{E} = \mathbf{E}_0 \mathrm{e}^{i(\mathbf{k}\cdot\mathbf{r}-\omega t)}. \tag{3.1}$$

$\mathbf{k}$ is the wave vector of the electromagnetic beam, ω is the angular frequency, $\mathbf{r}$ the position vector in space and t is the time. The complex amplitude vector, $\mathbf{E}_0$, contains both information on the absolute amplitude of the wave, the phase constant of the wave and the polarization of the wave. Materials have refractive index close to unity in the X-ray regime, which means that electromagnetic waves with these wavelengths consider the material almost similar to vacuum. This means that the polarization is perpendicular to the wave vector $\mathbf{k}$, which follows from Maxwells equations for electromagnetic waves in vacuum. The electric field is the real part of Equation 3.1. In this representation the electromagnetic wave is considered a plane wave, and this is normally a good approximation when dealing with X-ray scattering, because the wavelength is very small compared to the usual spot size. If one approximates the beam from the X-ray source with a Gaussian beam, the radius of curvature, R, is given by:

$$R(y) = y\left(1 + \left(\frac{y_0}{y}\right)^2\right) \text{[19]}. \tag{3.2}$$

Here y is the distance from the beam center, and $y_0 = \pi W_0^2/\lambda$ [19], is the Rayleigh range, where W_0 is the beam width at the beam center, and λ is the wavelength of the beam. The beam width is in the order $\sim 10^{-4}$ m, the wavelength is in the order of $\sim 10^{-10}$ m and the distance from the beam center is in the order of $\sim 10^{-1}$ m. This implies that the radius of curvature will be in the order of $\sim 10^{2}$ m. The area illuminated by the X-ray beam is in the same order as the beam width, and it is therefore a good approximation to consider the incoming X-ray beam to be a planar wave when it is interacting with a sample because the radius of curvature is so large that the incoming beam will seem planar over an area the size of the beam spot.

With these approximations, and considering a wave traveling in the y-direction and polarized in the z-direction in a Cartesian coordinate system, one can write the electric field of the incoming X-ray beam as

$$\mathbf{E} = E_0 \sin(k_y y - \omega t)\hat{\mathbf{z}}. \tag{3.3}$$

Since it has been mentioned that X-rays can be regarded as particles, a short description will follow regarding the subject. When quantifying the electromagnetic wave, one is visualizing a particle called the photon with quantum energy $E = hf$. E is the energy, h is Planck's constant and f is the frequency of the electromagnetic wave. Viewing X-rays in this manner is important when considering the creation of characteristic X-ray spectra from an X-ray source and inelastic scattering such as Compton scattering, but will not be handled in more detail here, since it will suffice to know that photons exist to understand the work that has been done in this thesis.

3.3 Scattering Theory

3.3.1 Fundamental Scattering Theory

The fundamentals of scattering theory lays on the fact that an electron will interact with an incoming electromagnetic beam, or photon, depending on which representation is most fitting. In most X-ray scattering experiments it is assumed that the scattering is elastic. This means that the scattered wave has the same wavelength as the incoming photon. When considering scattering from a single electron, one imagines that the incoming electromagnetic wave will act with a force on the electron, and hence start to accelerate it. This will again cause the electron to radiate according to [20]

$$\frac{dP}{d\Omega} = \frac{e^2}{16\pi^2\epsilon} \frac{|\hat{\mathbf{r}} \times (\mathbf{u} \times \mathbf{a})|^2}{(\hat{\mathbf{r}} \cdot \mathbf{u})^5}. \tag{3.4}$$

This equation describes that accelerated electric charges will be the source for an electromagnetic wave. Here $dP/d\Omega$ is the radiated power to an infinitely small solid angle centered around the radiating particle. ϵ is the electric permittivity of the medium the electron is situated in, e is the electric charge, $\hat{\mathbf{r}}$ is the unit vector in radial direction and $\mathbf{a}$ is the acceleration of the electron. $\mathbf{u} = c\hat{\mathbf{r}} - \mathbf{v}$ where c is the speed of light and $\mathbf{v}$ is the velocity of the electron .

If one assumes that the incoming electromagnetic wave has an electric field of the form in Equation 3.3, then, according to Newton's second law, the acceleration and velocity will be given by

$$\mathbf{a} = \frac{eE_0}{m_e}\sin(\omega t)\hat{\mathbf{z}} \tag{3.5}$$

$$\mathbf{v} = \frac{eE_0}{m_e\omega}\cos(\omega t + \alpha)\hat{\mathbf{z}}. \tag{3.6}$$

Here electrons located at $y = 0$ are considered. α is a phase constant and m_e is the electron mass. By including this in Equation 3.4 the radiated power per steradian is:

$$\frac{dP}{d\Omega} = \frac{e^4 {E_0}^2}{16\pi^2 \epsilon m_e^2 c^3} \frac{\sin^2\omega t_r \sin^2\theta}{(1 - \frac{eE_0}{m_e\omega c}\cos\theta\cos(\omega t_r + \alpha))^5}. \tag{3.7}$$

$t_r = t - r/c$ is the retarded time, accounting for the fact that the signal needs a finite time to travel the distance r. θ is the angle the radial unit vector forms with the z-axis. A single electron will thus give out electromagnetic radiation when accelerated by an electromagnetic wave. The fact that the scattered intensity goes as $1/m^2$, where m is the mass of the scattering particle, shows why only electrons are considered in X-ray scattering, and not protons. Protons have 2000 times the mass of an electron, and the scattering will therefore be very weak compared to the scattering from the electrons.

3.3.2 Scattering From Multiple Scatterers

When considering X-ray scattering it is not usual to look at scattering from a single electron, but from the sum of all electrons illuminated by the X-ray beam. This is because the electromagnetic waves from each accelerated electron can interact in either a destructive or constructive way, depending on the phases of the waves. To understand this, it is necessary to first look at the scattering from a single atom. The scattering intensity is proportional to the absolute square of the atomic form factor, f^0, given by the Fourier transform of the charge density $\rho(\mathbf{r})$ [21].

$$f^0 = \int \rho(\mathbf{r}) \mathrm{e}^{i\mathbf{q}\cdot\mathbf{r}} d\mathbf{r}. \tag{3.8}$$

$\mathbf{r}$ is the position vector in real space and the scattering vector $\mathbf{q}$ is given by

$$\mathbf{q} = \mathbf{k}' - \mathbf{k}, \tag{3.9}$$

where $\mathbf{k}'$ and $\mathbf{k}$ are the outgoing and incoming wave vectors, respectively. The scattering angle, 2θ, is the angle between the incoming and outgoing wave vector. When considering the scattering from multiple atoms, the sum is done over all the atom's atomic form factor, with the additional factor $\mathrm{e}^{i\mathbf{q}\cdot\mathbf{r}}$ to account for the fact that different atoms will spread with a different phase [22]. As the intensity of the scattering from a single atom is proportional to the atomic form factor, the intensity of the scattering from multiple atoms is proportional with the absolute square of the form factor, F, given by [21]

$$F(\mathbf{q}) = \sum_j f_j(\mathbf{q})\mathrm{e}^{i\mathbf{q}\cdot\mathbf{r}_j}. \tag{3.10}$$

Here the sum goes over all the different atoms involved, and $f_j(\mathbf{Q})$ is the atomic form factor of atom number j. By considering only identical atoms, the intensity, $I(\mathbf{q})$, is then given by:

$$I(\mathbf{q}) = |f(\mathbf{q})|^2 \sum_n \mathrm{e}^{i\mathbf{q}\cdot\mathbf{r}_n} \sum_m \mathrm{e}^{-i\mathbf{q}\cdot\mathbf{r}_m} = |f(\mathbf{q})|^2 \sum_n \sum_m \mathrm{e}^{i\mathbf{q}\cdot(\mathbf{r}_n-\mathbf{r}_m)}. \tag{3.11}$$

By separating the summation of $n = m$ from $n \neq m$, and in addition changing the summation over m by an integral over the electron density ρ_n, and finally adding and subtracting an integral over the average electron density, ρ_{at}, one arrives at the scattering intensity [21]

$$\begin{aligned} I(\mathbf{q}) = N|f(\mathbf{q})|^2 + |f(\mathbf{q})|^2 \sum_n \int_V [\rho_n(\mathbf{r}_{nm}) - \rho_{at}]\mathrm{e}^{i\mathbf{q}\cdot(\mathbf{r}_n-\mathbf{r}_m)} dV_m \\ + |f(\mathbf{q})|^2 \rho_{at} \sum_n \int_V \mathrm{e}^{i\mathbf{q}\cdot(\mathbf{r}_n-\mathbf{r_m})} dV_m. \end{aligned} \tag{3.12}$$

$\mathbf{r}_n$ is here a fixed reference position in the sample. The electron density at position $\mathbf{r}_{nm} = \mathbf{r}_m - \mathbf{r}_n$ will quickly approach the average electron density ρ_{at} for increasing $\mathbf{r}_{nm}$ if the material is not crystalline [21]. The second term in Equation 3.12 will therefore vanish for large $\mathbf{r}_{nm}$. The third term in Equation 3.12 will only contribute for small scattering vectors $\mathbf{q}$. This comes from the fact that when integrating over the volume the phase factor $\mathrm{e}^{i\mathbf{q}\cdot(\mathbf{r}_n-\mathbf{r_m})}$ will oscillate quickly along the unit circle and the integral will add up to zero unless $\mathbf{q}$ is small. Small $\mathbf{q}$ means small scattering angle 2θ, and this part of the signal is therefore considered the Small-Angle X-ray Scattering (SAXS) intensity, which gives information on the mesoscale average electron density variations throughout the sample investigated.

3.3.3 Small-Angle X-ray Scattering

Scattering Intensity in the SAXS Regime

The small-angle X-ray scattering intensity is formalized from Equation 3.12 as

$$I^{SAXS} = |f(\mathbf{q})|^2 \sum_n \mathrm{e}^{i\mathbf{q}\cdot\mathbf{r}_n} \int_V \rho_{at} \mathrm{e}^{-i\mathbf{q}\cdot\mathbf{r}_m} dV_m. \tag{3.13}$$

By doing a similar transformation from a sum to an integral as in Equation 3.12, the SAXS intensity becomes

$$I^{SAXS} = |f|^2 \int_V \rho_{at} \mathrm{e}^{i\mathbf{q}\cdot\mathbf{r}_n} dV_n \int_V \rho_{at} \mathrm{e}^{-i\mathbf{q}\cdot\mathbf{r}_m} dV_m. \tag{3.14}$$

This can be approximated by [21]

$$I^{SAXS} = |\int_V \rho_{sl} \mathrm{e}^{i\mathbf{q}\cdot\mathbf{r}} dV|^2, \tag{3.15}$$

if the form factor $f(\mathrm{q})$ varies little for small q. The variable $\rho_{sl} = f\rho_{at}$ have here been introduced and is called the scattering length density. In general the integration volume is over the entire sample. For particles in a low solution there is no ordering between the particles, and therefore no constructive or destructive interference arise because of the ordering. When this happens, the scattering intensity at small angles is given by the Fourier transform of the difference between the scattering length density of the particle and the surrounding material used as solvent [21]. If the scattering length density of the particle is uniform, then the intensity of the scattering signal from a single particle, I_1^{SAXS}, is given by

$$I_1^{SAXS}(\mathbf{q}) = (\rho_{sl,p} - \rho_{sl,0})^2 |\int_{V_p} \mathrm{e}^{i\mathbf{q}\cdot\mathbf{r}} dV_p|^2. \tag{3.16}$$

$\rho_{sl,p}$ and $\rho_{sl,0}$ is the scattering length density of the particle and the solvent. V_p is the volume of the particle. Since the volume integral is changed from the entire sample volume, to only over a single particle, the scattering intensity from the single particle has to depend on the difference between the scattering length density of the particle and the solution. This is because this intensity is how much the signal is modified compared to the signal from the pure solution. If the particle and the solution would have the same scattering length density, then one would not be able to see the particle in the scattering data, and I_1^{SAXS} would be equal to 0. With the single particle form factor

$$F(\mathbf{q}) = \frac{1}{V_p} \int_{V_p} \mathrm{e}^{i\mathbf{q}\cdot\mathbf{r}} dV_p, \tag{3.17}$$

which is the Fourier transform of the particle shape, $I_1^{SAXS}(\mathbf{q})$ becomes

$$I_1^{SAXS}(\mathbf{q}) = \Delta\rho^2 V_p^2 |F(\mathbf{q})|^2, \tag{3.18}$$

where $\Delta\rho$ is the difference in scattering length density of the particle and the solvent.

Polydispersivity

If the particles being imaged have various sizes, then the system is polydisperse. To get the correct intensity in the small-angle X-ray scattering regime, it it necessary to take a weighted sum of all the different particle sizes. If the distribution of the different particle sizes, R, is $D(R)$, then Equation 3.18 is modified to [21]

$$I(\mathbf{q}) = \Delta\rho^2 \int_0^\infty D(R) V_p(R)^2 |F(\mathbf{q}, R)|^2 dR \tag{3.19}$$

The size distribution is normalized such that

$$\int_0^\infty D(R) dR = 1. \tag{3.20}$$

This creates the effect that the scattering signal is smeared out, and characteristic peaks become smaller.

Form Factors for Different Shapes

For the study in this thesis talc particles have been studied. It is known from earlier studies of talc containing polypropylene that the talc particles form thin flakes oriented with their surface normals roughly parallel to the exterior surface normals of the sample [5].

Two different shapes were tested for finding the best fit for the shape of the talc flakes to the experimental data. These were a cylinder and a full spheroid. A visual representation of these can be seen in Figure 3.2

The form factor for the cylinder, F_{cy}, and the full spheroid, F_{fsph}, are given by [23]:

$$F_{cy}(\mathbf{q}', R, H) = 2\pi R^2 H \frac{\mathrm{J}_1(q_{||'}R)}{q_{||'}R} \mathrm{sinc}(q_{y'}H/2) e^{iq_{y'}H/2} \tag{3.21}$$

$$F_{fsph}(\mathbf{q}', R, H) = e^{iq_{y'}H/2} \int_0^{H/2} 4\pi R_{y'}^2 \frac{\mathrm{J}_1(q_{||'}R_{y'})}{q_{||'}R_{y'}} \cos(q_{y'}y') dy'. \tag{3.22}$$

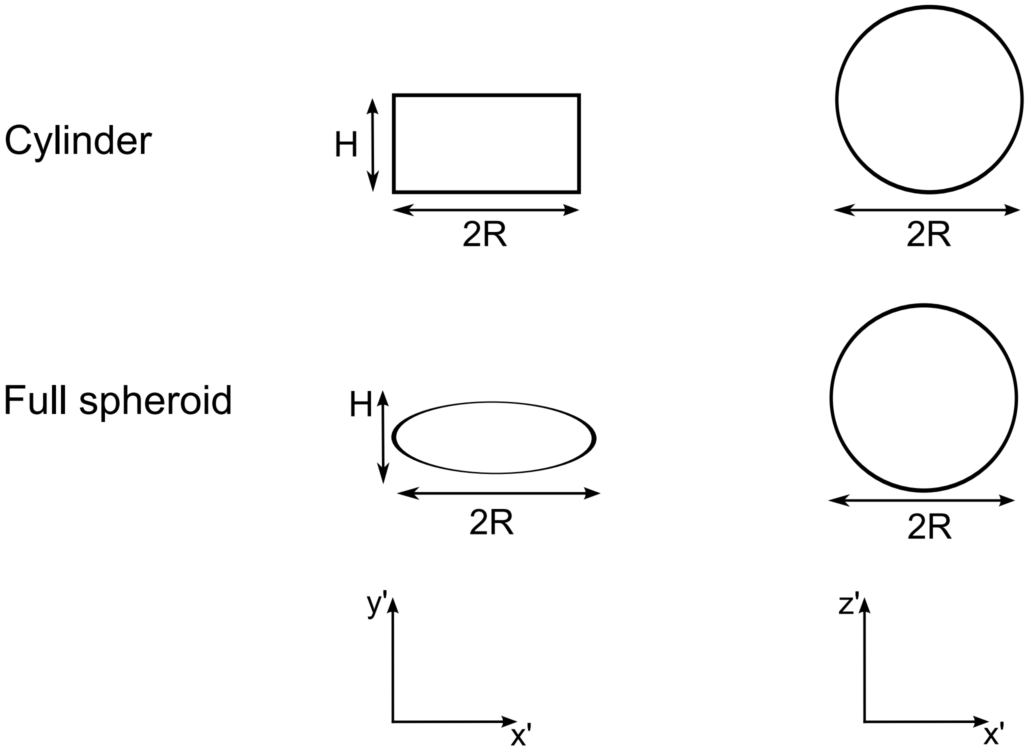

Figure 3.2: Two different shapes for modeling the geometry of a talc flake. Each shape is shown in two different planes, with different characteristic lengths indicated.

Here $\mathrm{J}_1(x)$ is the Bessel function of first order, and the other variables are given below with dimensions as indicated in Figure 3.2.

$$\begin{aligned} q_{||'} &= \sqrt{q_{x'}^2 + q_{z'}^2}, \\ R_{y'} &= R\sqrt{1 - 4\frac{y'^2}{H^2}} \end{aligned} \tag{3.23}$$

Structure Factor in the Sample

If the particle density is not sufficiently diluted to ignore the ordering among the particles, then the structure factor $|S(\mathbf{q})|^2$ has to be multiplied into Equation 3.18. $S(\mathbf{q})$ is here the Fourier transform of the function $s(x, y)$ describing how the particles are ordered. The small-angle scattering intensity then becomes [21]

$$I^{SAXS}(\mathbf{q}) = \Delta\rho^2 V_p^2 |F(\mathbf{q})|^2 |S(\mathbf{q})|^2. \tag{3.24}$$

The reason why the structure factor can be multiplied into the equation comes from the fact that the intensity is the Fourier transform of the electron density, which can be regarded as the convolution of the electron density of a single particle and some sort of perfect or imperfect lattice. Since

$$\mathfrak{F}(h * g) = H \cdot G, \tag{3.25}$$

where $\mathfrak{F}$ denotes the Fourier transform, h and g are real space functions, $*$ symbolizes the convolution and H and G denote the Fourier transforms of h and g, it is possible to simply multiply the structure factor with the form factor to the get the intensity.

3.4 Absorption

When X-ray beams travel through a material the intensity of the beam is attenuated because of absorption [21]. This absorption can for example be photoelectric absorption, where an electron absorbs a photon and is thereafter expelled from the atom. When considering the attenuation of an X-ray beam through a material, the intensity I after a distance l is given by:

$$I = I_0 e^{-\int_l \mu(s,t,z) dl'}, \tag{3.26}$$

where the integral is a line integral through the sample along l. I_0 is the initial intensity, and $\mu(s, t, z)$ is the spatially varying attenuation coefficient, which describes how much the material absorbs. The attenuation coefficient is in general varying in space and energy. The experiments this report is based on were done with a monochromatic beam at the Swiss Light Source. The energy dependence of the absorption coefficient is therefore not relevant for the continued work. The advantage of working with a monochromatic beam in computational tomography is that some complications, like *beam hardening*, will not appear. This will further be discussed in Section 3.5.3.

The absorption coefficient for a material in the X-ray regime is generally small for soft materials like plastic or tissue. However, it is in many cases important to correct for this effect. Especially when the X-ray beam the analysis is based on travels through significant different lengths in a sample. Correcting for the absorption can be done by multiplying the measured intensity I with the factor $\exp(\int_l \mu(s, t, z) dl)$. This will give the incoming intensity I_0. One important thing to notice is that this does not only apply to the direct incoming beam, from for instance an X-ray source. The scattered beams in a sample will also be attenuated in the same manner. To know how much of the wave was scattered, corrections have to be made to the measured signal.

3.5 Computational Tomography

3.5.1 Filtered Backprojection

Computational tomography is a method to image the the interior of a sample. This sample could for example be the human body, or a sample of polypropylene, as it is in this case. By using computational tomography it is possible to see how different structural variables change with position inside a sample, depending on what the imaging parameter is. The procedure is done by making projections of the sample at different angles, and then recreating the imaged variable.

The classical way of doing X-ray tomography is by imaging the absorption coefficient, μ, and this will be used to facilitate in explain how computational tomography is performed. When X-rays travel through a sample, the direct beam will be attenuated due to absorption and scattering in the sample. After transversing a distance in a sample, the incoming intensity, I_0, will, as previously stated, be attenuated according to equation 3.26. By taking the natural logarithm of the incoming intensity divided by the outgoing intensity the attenuation coefficient becomes projected along the beam path y:

$$p(x, \psi) = \ln\left(\frac{I_0}{I}\right) = \int_y \mu(s,t)dy. \tag{3.27}$$

$p(x, \psi)$ is here the radon transform of the attenuation coefficient μ for different angles, ψ, in the tomography scan. By measuring the attenuated beam leaving the sample for different places, x, the projection profile of the sample is obtained. Figure 3.3 demonstrates how the projection profile is acquired for different angles. The sample is illustrated by the dotted line and within this sample there are two regions with high attenuation coefficient. It is done one projection for each step interval of x along the line y, and for different values of ψ, according to Equation 3.27. This yields the function $p(x, \psi)$ which is called the radon transform of μ for the given angle ψ. Reconstructing the function $\mu(s,t)$ is often done by taking the Fourier transform of the radon functions, and then utilizing the Fourier slice theorem. This is seen by taking the two dimensional Fourier transform of the function $\mu(s,t)$:

$$M(\nu) = \int_{-\infty}^{\infty}\int_{-\infty}^{\infty} \mu(s,t)e^{-i2\pi\mathbf{\nu}\cdot\mathbf{r}}dsdt. \tag{3.28}$$

Instead of integrating along the s- and t-axis, the x- and y-axis, tilted an angle ψ compared to the original frame, are utilized, as demonstrated in

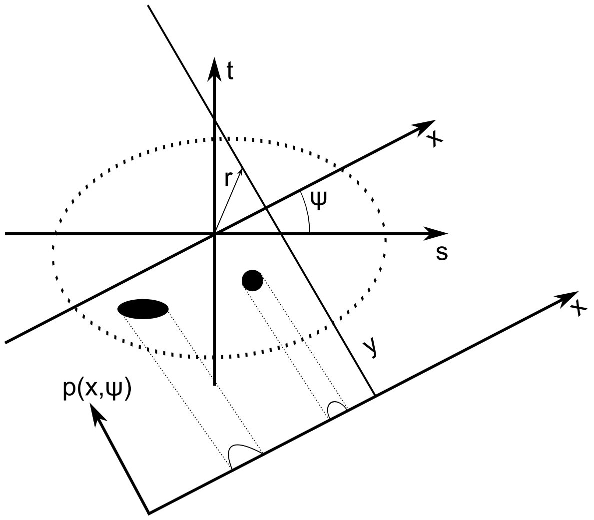

Figure 3.3: The projections through a sample (outlined by the dotted line) with two areas of high attenuation, symbolized by the black regions. The projection is done along the line y normal to the x-axis which forms an angle ψ with the s-axis. Multiple projections for different x-values and different ψ values construct the function $p(x, \psi)$.

Figure 3.3. The Fourier transform can then be written:

$$M(\nu_x, \nu_y) = \int_{-\infty}^{\infty} \int_{-\infty}^{\infty} \mu(s,t) e^{-i2\pi(\nu_x x + \nu_y y)} dy dx. \tag{3.29}$$

Setting the component $\nu_y = 0$ is the same as looking at how the Fourier transform looks along the x-axis. The two-dimensional Fourier transform for this case will be

$$M(\nu_x, 0) = \int_x \left[\int_y \mu(s,t) dy \right] e^{-i2\pi\nu_x x} dx = \int_x p(x, \psi) e^{-i2\pi\nu_x x} dx = P(\nu_x, \psi), \tag{3.30}$$

where Equation 3.27 has been substituted in, and $P(\nu_x, \psi)$ is the Fourier transform of $p(x, \psi)$. This means that the Fourier transform of the one dimensional projection $p(x, \psi)$ is the Fourier transform of the function $\mu(s, t)$ along a line passing through the origin and forming an angle ψ with the s-axis. The Fourier components will then lie on a line with an angle ψ compared to the ν_s axis, which is demonstrated in Figure 3.4. By doing different projections for different angles the values in ν-space would be filled up. It could then be possible to do an inverse Fourier transform for these data to acquire the function $\mu(s, t)$. A direct inverse Fourier transform would

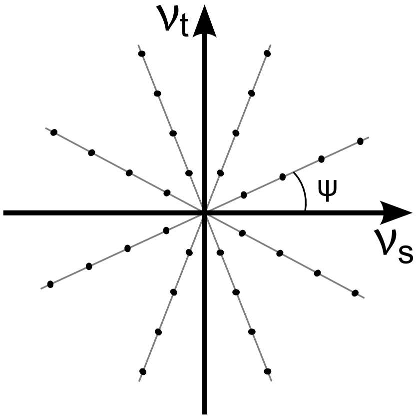

Figure 3.4: Representation of the Fourier slice theorem. Each line at different angles ψ represents the Fourier transform of a projection function $p(x, \psi) = \int_y \mu(s,t)dl$, where dy is along a line tilted a value $\psi + 90°$ compared to the s-axis. Since the measurements done are of finite sampling rate only certain values are known in the frequency space ν. These are indicated by the black marks.

however require an infinite number of angles, and an infinite small step length along the x-axis to get the correct result. Only a finite number of values will be known for the frequency domain since the sampling rate in the frequency domain is $1/\Delta x N$[1], where Δx is the step length along the x-axis and N is the number of projections obtained. Different methods are used to get around this problem. One method commonly used is *filtered backprojections* [1]

$$\mu(s,t) = \int_0^{\pi} \left(\int_{-\infty}^{\infty} P(\nu, \psi) e^{i2\pi\nu t} |\nu| d\nu \right) d\psi, \tag{3.31}$$

and is used in this project. This transform is an ordinary inverse Fourier transform in polar coordinates. $|\nu|$ in Equation 3.31 should be exchanged with a filter function, $S(\nu)$. A common filter to apply is the filter $S(\nu) = 0$ for $|\nu| > \nu_{\max}$ and $|\nu|$ elsewhere. This filter is called a Ram-Lak filter. The value of $\nu_{\max}$ is decided by the sampling distance Δx. The highest spatial frequency it is possible to observe is the Nyquist frequency $\nu_{\max} = 1/2\Delta x$ [1]. It can in addition be applied a number of other filters, depending on the desired output. The filter used in this project is the Ram-Lak filter multiplied with the Hamming filter. This filter is

$$S(\nu) = \begin{cases} |\nu|(0.54 + 0.46\cos\left(2\pi\Delta x\nu N/(N-1)\right)) & |\nu| < \nu_{\max} \\ 0 & |\nu| > \nu_{\max} \end{cases} \tag{3.32}$$

Δx is the interval along the x-axis where the projections are measured. This has the effect that the higher frequencies are weighted less, and since noise in the picture have high frequencies, this filter will suppress some of the noise. The entire backprojection is then given by:

$$\mu(s,t) = \int_0^{\pi} \left(\int_{-\infty}^{\infty} P(\nu,\psi) e^{i2\pi\nu x} S(\nu) d\nu \right) d\psi. \tag{3.33}$$

In the practical implementation a fast Fourier transform (FFT) and an inverse fast Fourier transform (IFFT) routine are used because only a finite number of transmissions are measured. The Fourier transform of Equation 3.27 is approximated by [1]

$$P(\nu_n,\psi) = \Delta x \cdot \mathrm{FFT}\{p(x_n,\psi\}, \tag{3.34}$$

where n is an integer representing the n'th sampled value. The innermost integral in Equation 3.33 is then given by [1]:

$$\begin{aligned} Q_\psi(x) = \int P(\nu,\psi) S(\nu,\psi) e^{i2\pi\nu x} d\nu &\approx \Delta\nu \sum_n P_n S_n e^{i2\pi\nu_n x_n} \\ &= \Delta\nu N \cdot \mathrm{IFFT}\{P(\nu_n,\psi) \cdot S(\nu_n)\}. \end{aligned} \tag{3.35}$$

Here the extra N, comes from the normalization in the IFFT-routine implemented in `Matlab`. $\Delta\nu = 1/N\Delta x$. By introducing dimensionless variables $\chi = x/\Delta x$ and $\omega = \nu \cdot \Delta x$ the problem becomes dimensionless, and can be implemented with ease on a computer. $Q_\psi(x)$ will then be written [1]

$$Q_\psi(x) = \frac{1}{\Delta x} \mathrm{IFFT}\{\mathrm{FFT}\{p(\chi_n,\psi)\} S(\omega_n,\theta)\} \tag{3.36}$$

The backprojection is then the outer integral in Equation 3.33 and can be approximated by [1]

$$\mu(s,t) = \frac{\pi}{K} \sum_{i=1}^{K} Q(s\mathrm{cos}(\psi_i) + t\mathrm{sin}(\psi_i)). \tag{3.37}$$

The distance $x = s\mathrm{cos}(\psi_i) + t\mathrm{sin}(\psi_i)$ can easily be deduced from Figure 3.3. For the cases where the value $s\mathrm{cos}(\psi_i) + t\mathrm{sin}(\psi_i)$ does not match one of the measured points x along the x-axis, simple interpolation between the closest points has been used.

3.5.2 Sinograms

A very helpful tool when working with tomography is the sinogram. This is a plot showing the value of each projection step, and how it varies for the different angles. The name sinogram gives an indication of what the plot will look like. As the sample is rotated with respect to the laboratory frame a feature will move with respect to the x-axis as indicated in Figure 3.3. Each feature will trace a line which resembles a sine wave in the plot. To illustrate this the radon transforms of an image with a single feature, shown in Figure 3.5 (a), have been taken. The sinogram of these projections is shown in Figure 3.5 (b). The feature will move with respect to the x-axis as the sample is rotated, and this creates a sine-shaped wave. A sinogram is also often helpful to spot errors in the experimental procedure. If the sample has suddenly moved during the imaging, then this will show up as a discontinuity in the sinogram.

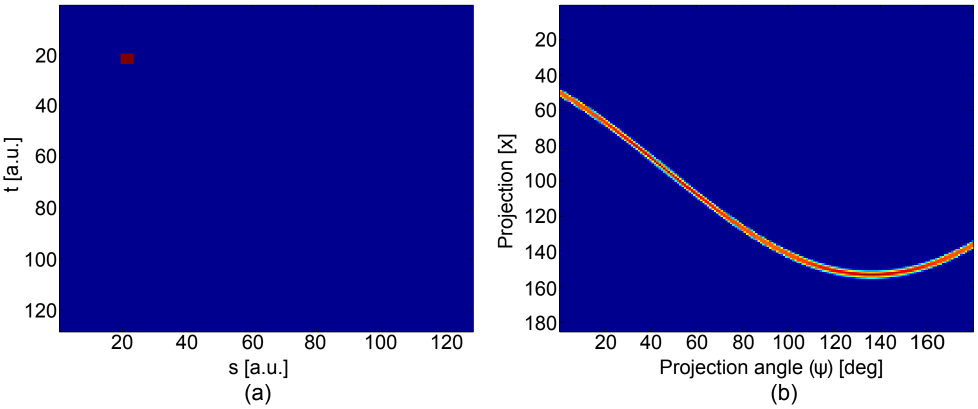

Figure 3.5: The radon transform of the image in (a) has been taken, and the corresponding sinogram is shown in (b). The single feature in the image creates a sine-shaped.

3.5.3 Image Artifacts

When working with tomography, there are a number of different artifacts which can appear in an image. Some of these are quite easy to correct, while others can only be approximately corrected, and can be due to resolution limitations. Some typical artifacts encountered when performing tomography will be presented in this section.

Beam Hardening

It was previously noted that beam hardening is a type of artifact which can appear doing computational tomography. This is not directly relevant for this case, because the experiment performed was done with a close to perfectly monochromatic beam, but since it was mentioned it will very briefly be described here.

When measuring the attenuation coefficient with computational tomography the physical measured quantity is the attenuation of the X-ray beam. Since the attenuation coefficient is different for different energies of the X-rays this can lead to beam hardening. This means that the soft X-rays (X-rays with lower energy) will be absorbed in a higher degree than the hard X-rays. If a sample contains a region with a much higher attenuation coefficient than the rest of the sample, then the beam which travels through this area will have its spectrum's center of mass shifted to much higher energies. The attenuation will then look to have been higher for the entire sample along the beam path. This beam hardening artifact can be very dominant between two areas of high attenuation coefficient. The beam hardening artifact can be seen in Figure 3.6. Here, the area between the two regions with high attenuation, white circles, is darker than the surroundings, although it is only two kind of materials in the sample, the white area with high attenuation, and the grey area with lower attenuation.

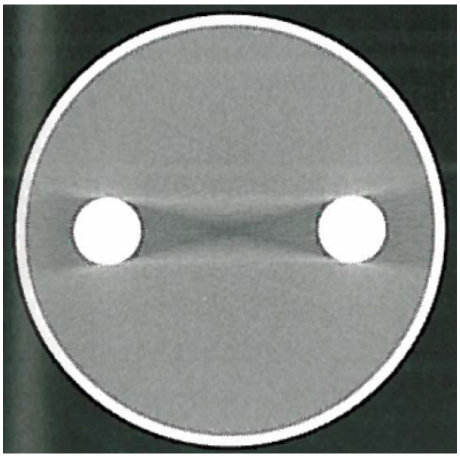

Figure 3.6: The effect of beam hardening can be seen between the two areas with high attenuation coefficient, marked with white. Figure adapted from a NTNU course[1]

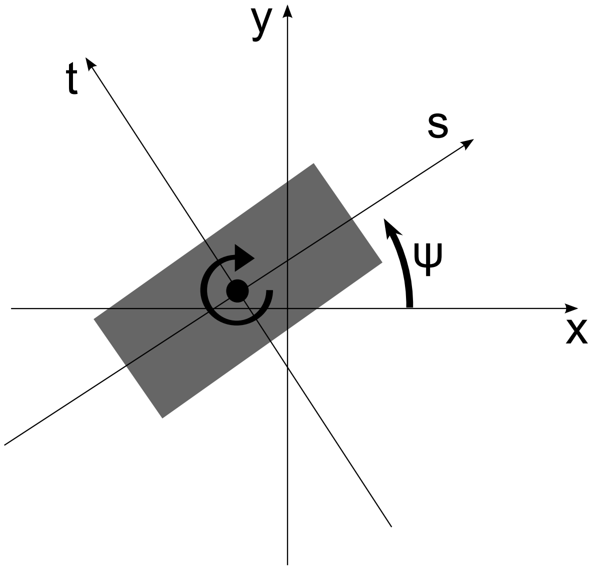

Figure 3.7: Illustration of misalignment of the rotation axis of the sample frame with the fixed laboratory frame.

Misalignment Artifacts

The most pronounced artifacts in the experiment performed are the occurrence of artifacts caused by movement of the sample and misalignment of the rotation axis of the sample compared to the origin of the xy-plane in the laboratory frame. If the origin of the sample frame is shifted compared to the laboratory frame, as is the case in Figure 3.7, then this will lead to problems with the backprojection, because the relation between the x-coordinate, the ψ-angle and the (s,t)-coordinates in Equation 3.37 does not hold. This relation says that the coordinates $(s,t) = (0,0)$ have to be $x = 0$ for all angles ψ. Movement of the sample is usually not a big concern when doing experiments on non-living samples. The samples can however move a little during the scan, caused by drifts in the motors it is attached to. The artifact this problems leads to is smearing of edges, because a region will be back projected to different places in the (s,t)-plane.

To correct for this misalignment, it is possible to shift each sinogram in such a way that the axis of rotation coincides with the origin of the laboratory frame. This is however difficult, since it would require very precise measure-

---

[1] The course TFY4320 Medical Physics contained several figures regarding CT and artifacts, including this one.

ment of the rotation axis. This would be equally difficult as aligning the axis of rotation in the first place, and is therefore not the best suited option. The method used in this report has been to align the sinogram according to the center of mass of each projection of the attenuation coefficient, which is measured by the attenuation of the direct beam. By shifting the center of mass of each projection to the origin of the laboratory frame, it is made sure that one point of the sample does not move out of the origin of the laboratory frame. Thus it is chosen that the center of mass is also the axis of rotation and that it is aligned with the laboratory frame. How the center of mass alignment works is demonstrated in Figure 3.8. One implication of aligning the sinograms according to the center of mass is that this shifts the entire reconstructed sample towards the center of the tomogram. An example of how the sample image move when aligning the sinogram is given in Figure 3.9

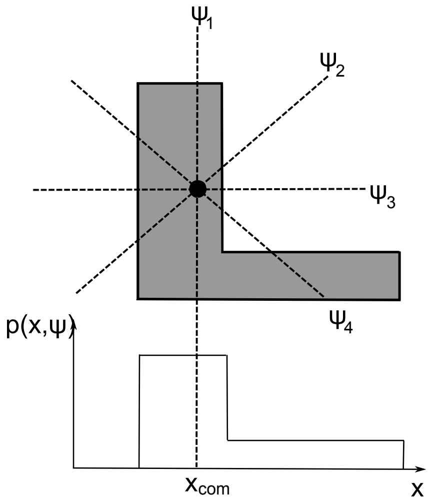

Figure 3.8: By aligning the center of mass (x_{com}) of each projection ($p(x, \psi)$) of the attenuation coefficient of the sample, grey area, to the axis of rotation, and also aligning the axis of rotation to the laboratory frame, it is made sure that the sinogram is properly aligned. When this is done; one point, the black point symbolizing the center of mass, will stay at the origin of the laboratory frame for all angles. This is easy to see because x_{com} has to go through the center of mass of the sample for all the different angles of ψ_i.

The effect of how a tomogram looks before and after alignment can be seen in Figure 3.10. This figure indicates that correcting for movement and misalignment is important to get a clear image.

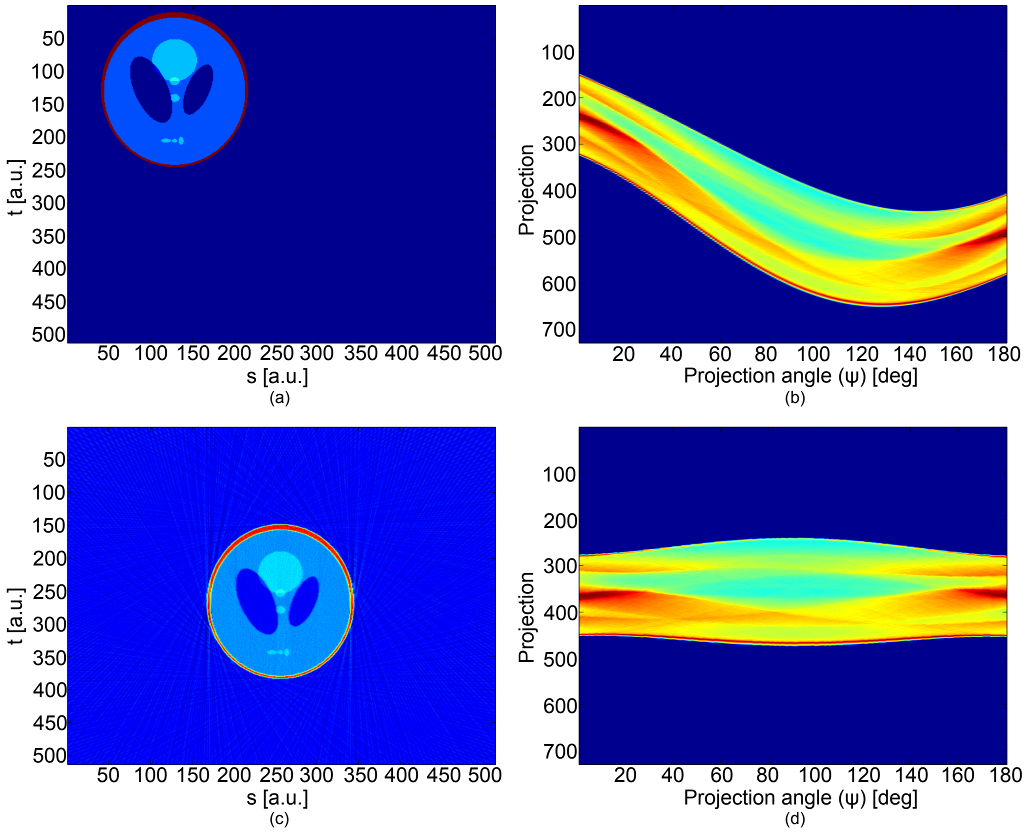

Figure 3.9: Illustration of how the image will move when the sinogram is aligned using the center of mass. (a) The original image, (b) the radon transforms of the image, (c) the backtransform of the image after alignment of the sinogram, (d) alignment of sinogram according to the center of mass.

Streak Artifacts

Streak artifacts are straight lines in the reconstructed tomogram which should not be there. These will occur if there are faults with the imaged values in the sinogram. If for instance the flux in the X-ray beam suddenly increases for one single projection, this will cause inconsistencies in the sinogram. Undersampling and poor counting statistics are also factors which contributes to these inconsistencies. Figure 3.11 shows how a streak artifact looks in a tomogram, compared to the tomogram reconstructed from a perfect sinogram.

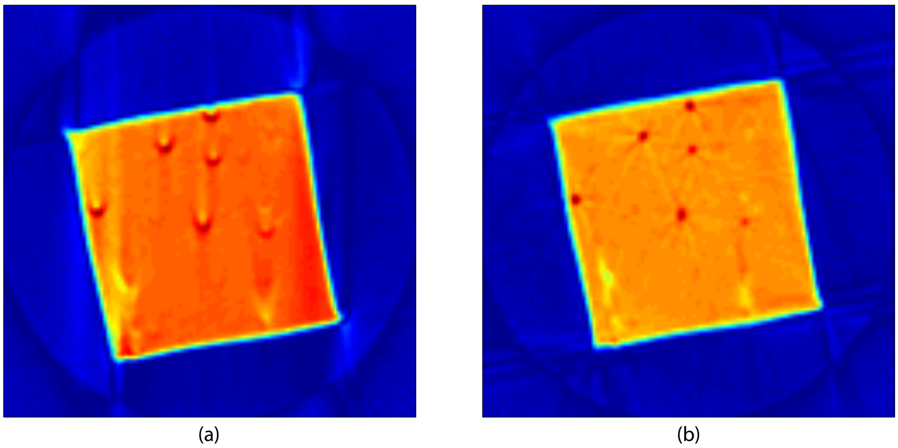

(a)

(b)

Figure 3.10: The figures show the difference between the reconstructed tomograms before (a) and after (b) alignment of the sinogram. The areas with high attenuation, which give the dark red spots in (b), are smeared out in the uncorrected tomogram (a).

3.6 Scattering Cross-Section

When doing a scattering experiment, as shown in Figure 3.12, the scattering cross section is a useful quantity. This tells how likely it is that a particle, for instance a photon, will be scattered by another particle. In general, if a particle hits a sample containing only equal particles, with number density $n(s, t, z)$, then the scattered intensity into a detector will be [21]

$$I_{sc} = I_0 N \Delta\Omega \left(\frac{d\sigma}{d\Omega} \right). \tag{3.38}$$

Here, I_{sc} is the scattered intensity, I_0 is the incoming intensity hitting the sample, N is the particles in the sample per unit area seen along the beam direction, $\Delta\Omega$ is the solid angle which the detector surface constitutes with the sample as center, and $d\sigma/d\Omega$ is the differential cross-section. Equation 3.38 does not account for absorption in the sample, and a term accounting for this should be added if the sample is of considerable thickness compared to the attenuation length. If the sample does not contain particles with identical scattering cross sections, the scattered radiation when a beam travels through a sample will be

$$I_{sc} = \int_l I_0 n(s, t, z) dl \Delta\Omega \frac{d\sigma(s, t, z)}{d\Omega}. \tag{3.39}$$

Here it is assumed that $n(s, t, z)dl$ is a good approximation to the two dimensional particle density N. This should be a fairly good approximation when

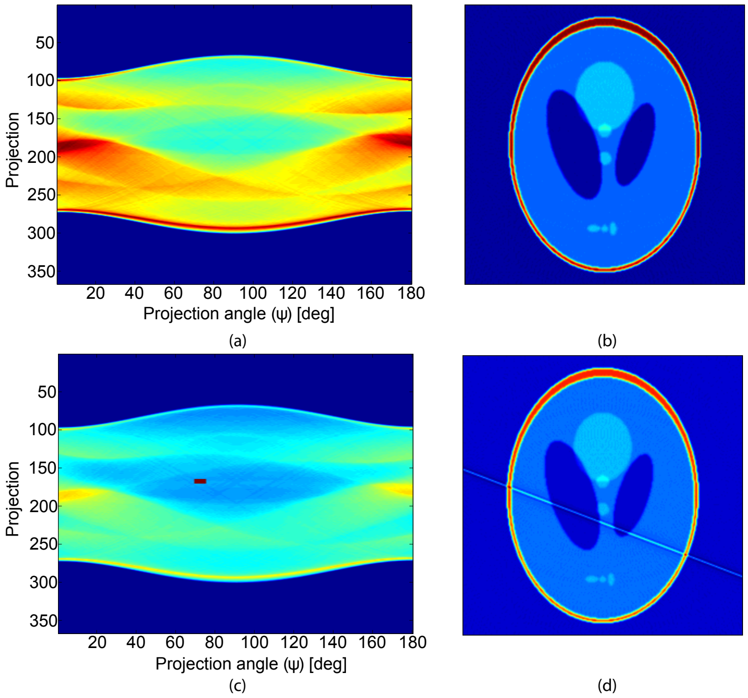

Figure 3.11: The perfect sinogram in (a) gives the tomogram (b). In (c) some fault with the experiment has caused one pixel in the sinogram to have a much higher value than it should, marked with the dark red color. When recreating the tomogram from these data, a clear line in (d) is observed, which should not be there and is considered a *streak artifact.*

the relative change in particle density is much smaller than unity, over a distance W, which is the width of the beam, $W|\nabla n|/n << 1$. Since it is more useful to work with scattering vectors than solid angles in X-ray scattering, Equation 3.39 can be rewritten, by using

$$\begin{aligned} q &\propto \sin(\theta) \\ dq &\propto \cos(\theta) d\theta \end{aligned} \tag{3.40}$$

and inserting this for the expression of the solid angle:

$$\begin{aligned} d\Omega &= \sin(2\theta) d\theta d\zeta \\ d\Omega &= 2\sin(\theta)\cos(\theta) d\theta d\zeta \\ d\Omega &\propto 2q dq d\zeta, \end{aligned} \tag{3.41}$$

as

$$I_{sc} = \int_l I_0 n(s,t,z) dl \Delta q \Delta\zeta \frac{d\sigma(s,t,z)}{dq d\zeta}. \tag{3.42}$$

dq is now the thickness of the red scattering ring in Figure 3.12, and 2θ is in this case the scattering angle.

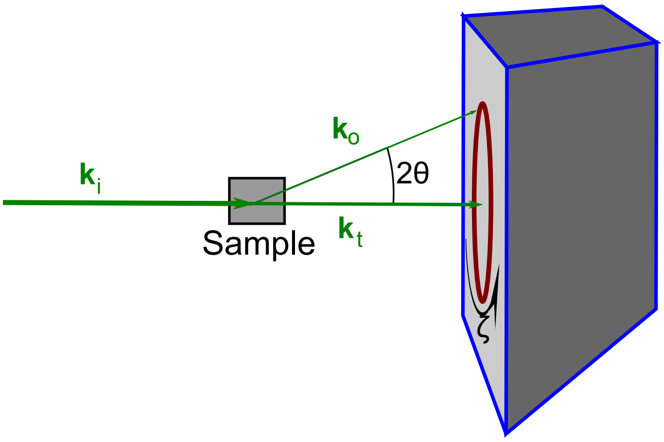

Figure 3.12: A typical scattering experiment. The vector $\mathbf{k}_i$ is the incoming wave vector and is scattered in the grey sample, which gives an outgoing wave vector $\mathbf{k}_o$. $\mathbf{k}_t$ is the transmitted wave vector which is not scattered by the sample. The scattered wave will hit the detector and form a pattern marked by a red ring. This pattern does not need to be a full ring, but is marked as such for simplicity. The scattering angle, 2θ, and the azimuthal angle, ζ, indicate how they are oriented in the scattering experiment.

3.7 SAXS Tomography

3.7.1 Imaged Variable

When reconstructing an image based on the small-angle scattering signal the routine for reconstructing the tomogram is identical for that of reconstructing the attenuation coefficient of the sample. The difference is in what the imaging variable is. To the first Born approximation, the SAXS pattern is given by Equation 3.42, when also considering absorption this takes the form [4]

$$I_{\mathbf{q}}(x,\psi) = I_0 \int_l dl f(\psi,x,l) \left[n\Delta q \Delta\zeta \frac{d\sigma(s,t)_{\mathbf{q},\psi}}{dqd\zeta} \right] g(\psi,x,l). \tag{3.43}$$

The integral is along the line l which follows the incoming X-ray beam to the position (s,t) in the sample where parts of the beam is scattered, according to the scattering cross section, and then leaves with an angle 2θ with respect to the incoming beam. The absorption in and out from the point (s,t) in the sample where the photon is scattered is given by the functions [4]

$$\begin{aligned} f(\psi,x,l) &= e^{-\int_{-\infty}^{l} dl'\mu(s,t)} \\ g(\psi,x,l) &= e^{-\int_{l}^{\infty} dl'\mu(s,t)}. \end{aligned} \tag{3.44}$$

$I_{\mathbf{q}}(x,\psi)$ is the scattered radiation measured on a detector at scattering vector $\mathbf{q}$, when the X-ray beam is at position x in the laboratory frame, and the sample is rotated an angle ψ. See Figure 3.1 for explanation of the coordinates. If the scattering angle 2θ is small, then one can approximate the direction of the scattered signal to be along the direction of the incoming X-ray beam, meaning that the line l in Equation 3.43 and 3.44 is just along the y-direction. The absorption part in Equation 3.43 can then be pulled out of the integral because every scattered beam travels along the same direction:

$$I_{\mathbf{q}}(x,\psi) = I_{x,\psi}\int_{y} dy\left[n\Delta q\Delta\zeta\frac{d\sigma(s,t)_{\mathbf{q},\psi}}{dqd\zeta}\right]. \tag{3.45}$$

$I_{x,\psi}$ is here the transmitted intensity through the sample. By dividing the scattered intensity, $I_{\mathbf{q}}$, by the transmitted intensity the radon transform of the differential SAXS cross section is obtained [4]

$$\frac{I_{\mathbf{q}}}{I_{x,\psi}} = \int_{y} dy\left[n\Delta q\Delta\zeta\frac{d\sigma(s,t)_{\mathbf{q},\psi}}{dqd\zeta}\right]. \tag{3.46}$$

The variable imaged when performing computational SAXS tomography would then be $n\Delta q\Delta\zeta(d\sigma(s,t)_{\mathbf{q},\psi}/dqd\zeta)$.

The challenge with this approach is that the sample is rotating. $d\sigma/dqd\zeta$ depends on the scattering vector $\mathbf{q}$ and when rotating the sample, the scattering cross section in the horizontal plane will change. This is seen when looking at a fixed position (s,t) in the sample and examining how the scattering cross section depends on the rotation angle. In Figure 3.13 it can be seen how the horizontal scattering vector in the laboratory frame, $\mathbf{q} = q\hat{\mathbf{q}}_x$, relates to the internal coordinate system of the sample, $(\mathrm{q_s},\mathrm{q_t})$. When the sample is rotated an angle ψ, the horizontal scattering vector in the laboratory frame will be the scattering vector $q_x\cos(\psi)\hat{\mathbf{q}}_{\mathbf{s}}+q_x\sin(\psi)\hat{\mathbf{q}}_{\mathbf{t}}$ in the sample frame.

When looking at the horizontal q-dependency of the scattering cross section in Equation 3.46 it can be seen how one line scan through the sample

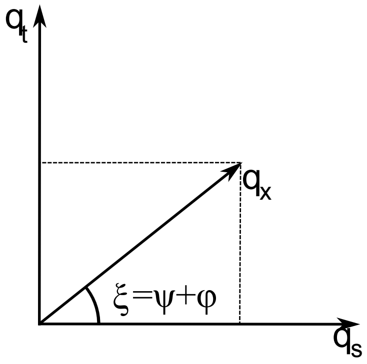

Figure 3.13: The figure indicates how the horizontal scattering vector in the laboratory frame, $\mathbf{q} = q\hat{\mathbf{q}}_x$, looks in the coordinate system of the sample, which is rotated an angle ψ compared to the laboratory frame.

will depend on the rotation angle ψ.

$$\frac{I_{q_x,\psi}}{I_{x,\psi}} = \int_y dy \left[n\Delta q\Delta\zeta \frac{d\sigma(q_x\cos(\psi))\hat{\mathbf{q}}_{\mathbf{s}} + q_x\sin(\psi)\hat{\mathbf{q}}_{\mathbf{t}})}{dqd\zeta} \right]. \tag{3.47}$$

Ordinary tomographic reconstruction is based on the assumption that each voxel at position (s, t) in the sample contributes equally much to the imaged variable in each projection that passes through that voxel, for all angles. From Equation 3.47 it is seen that the imaged value in each position (s, t) will change for each different angle ψ because the scattering vector in the sample frame will change. Therefore, the ordinary tomographic reconstruction algorithms will not work in reconstructing the horizontal components of the image variable presented in Equation 3.46. The component of the scattering cross-section parallel to the rotation axis is however independent of the rotation angle, and thus the q_z-component of the scattering cross section will not change while the sample rotates. It will therefore be possible to retrieve this component of the scattering cross section using ordinary filtered backprojection in a 2D plane of the sample.

This section has focused on imaging using components of the scattering cross section. This has been done because this is a more general case, and is valid for all systems where scattering is present. For the case of small-angle X-ray scattering the scattering is dependent on the form factor of the particle as shown previously. This gives however no different results or equations, since the scattering cross section is proportional to the form factor of a particle in the SAXS regime.

3.8 Simulated Annealing

Simulated annealing is a numerical method for finding the minimum of a function. This method is suitable for problems of large scale with many variables and where the global minimum is hidden among many poorer, local minimum [24]. The idea is to construct some function, E, which is to be minimized and then to perform Monte Carlo steps according to the probability distribution [24]

$$p \propto \exp(-E/T). \tag{3.48}$$

The function E is referred to as the energy of the system, while the parameter T is referred to as the temperature. A Monte Carlo step is to make a random step in the configuration space of the function which is supposed to be minimized. The old configuration is denoted E_α and the new configuration is denoted E_β. The probability of being in either of these configuration is p_α and p_β, given by Equation 3.48. If p_β/p_α is smaller than some random number, then the system is set equal to the new configuration, if p_β/p_α is bigger or equal to the random number, then the system stays in the old configuration. The strength of this method is that only the ratio between the probabilities is needed, and not the entire probability function with the normalization constant which is often impossible to find [2].

The algorithm works by performing cycles. Each cycle starts by performing a sufficient amount of Monte Carlo steps. If the energy, E, is smaller than at the beginning of the cycle the temperature T is set equal to T_{new}, where $T_{\text{new}} = T \cdot \delta T$, and $0 < \delta T < 1$. If it is not, then the cycle starts over without changing the parameter T. This cycle is repeated as long as necessary to obtain the desired solution.

The advantage of this method is that it should be able to avoid local minimum. If the function reaches a local minimum, it should be able to come out of this if the T-parameter is large enough, but when T is gradually lowered, it will no longer be able to make large steps towards a configuration with higher value for the function E, and thus settle toward the closest minimum. Since the system can move basically across all of configuration space at the start of the cycle, it is a higher probability that the minimum which is found in the end is the true global minimum of the function than if the method went to the nearest local minimum it could find from the initial starting condition.

---

[2] According to the lecture notes handed out by Alex Hansen in the course TFY4235 Computational Physics at NTNU

3.8.1 Reconstructing Using Linear Set of Equations

Formulating the Scattering Problem

If the shape and size of the particles involved in the scattering experiment are known, then the form factor is also known. It should then be possible to reconstruct the orientation distribution based on the recorded scattering image registered by the detector in Figure 3.12.

It will be assumed that the particles involved will have a preferred orientation along one of the axis in the sample. Thus the only variable to determine the full 3D orientation of the particle will be the angle between the x'-axis of the talc particle and the s-axis of the sample frame. This angle is called ϕ, and how it varies with position in the sample gives the orientation distribution $\phi(s, t)$. If particles have such an orientation distribution it should be possible to retrieve the orientation distribution by measuring the horizontal scattering in the laboratory frame.

We will now assume that the sample consist of n regions where it is assumed that the talc particles have only one orientation. This orientation is given by the angle, ϕ_m, between the x'-axis of the particle frame, and the s-axis of the sample frame. n is a whole number. The particles will be considered to scatter independently and the final scattering pattern will be corrected for absorption by dividing the scattered intensity by the transmitted intensity according to Equation 3.45. The intensity distribution on the detector, $I(\mathbf{q})_{x,\psi}$, when performing a scattering experiment on the sample at position x and angle ψ is assumed to take the form

$$I(\mathbf{q})_{x,\psi} = a_{\phi_1,x,\psi} I_{\phi_1,\psi}(\mathbf{q}) + a_{\phi_2,x,\psi} I_{\phi_2,\psi}(\mathbf{q}) + ... + a_{\phi_n,x,\psi} I_{\phi_n,\psi}(\mathbf{q}), \qquad (3.49)$$

when neglecting absorption. Here $I_{\phi_m,\psi}$ is the scattering intensity per unit length in region m (where the orientation is ϕ_m) when the angle in the tomography scan is ψ, and the scattering intensity is proportional to the absolute square of the form factor of the particle. $a_{\phi_m,x,\psi}$ is the length the X-ray beam travels through the region where the angle is ϕ_m. This means that the scattering pattern seen on the detector screen is equal to the sum of the products between the scattering intensity per unit length and the distance it travels through that region, for all the regions the X-ray beam travels through. Figure 3.14 illustrates the idea of how the scattering pattern is constructed when the X-ray beam travels through only two different regions in the sample.

In theory it should be enough to choose n different intensity values, for different $\mathbf{q}$, to solve for all the different coefficients $a_{\phi_m,x,\psi}$. The set of equations

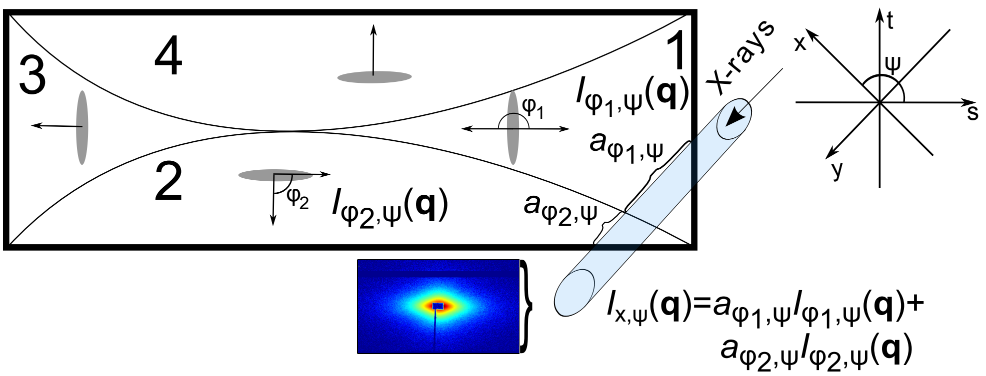

Figure 3.14: The figure illustrates the idea of how the scattering pattern is formed when the X-ray beam travels through the sample. The scattering pattern consist of two terms. One term is the product of the distance, $a_{\phi_1,\psi}$, the beam travels through region 1 and the scattering intensity, $I_{\phi_1,\psi}$, of particles with the given orientation ϕ_1 when the angle in the tomography scan is ψ. The second term is the similar product, but changing region 1 with 2. The two coordinate systems give the orientation of the sample compared to the laboratory frame.

which is to be solved is represented in matrix form as

$$I(\mathbf{q})_{x,\psi} = S_\psi \cdot a_{x,\psi}. \tag{3.50}$$

$I(\mathbf{q})_{x,\psi}$ is the recorded intensity as a function of scattering vector $\mathbf{q}$ at position x in the laboratory frame and angle ψ between the laboratory frame and the sample frame:

$$I(\mathbf{q})_{x,\psi} = \begin{bmatrix} I_{x,\psi}(q_1) \\ I_{x,\psi}(q_2) \\ \vdots \\ I_{x,\psi}(q_n) \end{bmatrix}. \tag{3.51}$$

We refer to S_ψ as the scattering matrix where each column is the scattering intensity vector $I_{\phi_i,\psi}(\mathbf{q})$, i = 1,2,..n, for each of the different orientation regions in the sample:

$$S_\psi = \begin{bmatrix} I_{\phi_1,\psi}(q_1) & I_{\phi_2,\psi}(q_1) & \dots & I_{\phi_n,\psi}(q_1) \\ I_{\phi_1,\psi}(q_2) & I_{\phi_2,\psi}(q_2) & \dots & I_{\phi_n,\psi}(q_2) \\ \vdots & \vdots & \ddots & \vdots \\ I_{\phi_1,\psi}(q_n) & I_{\phi_2,\psi}(q_n) & \dots & I_{\phi_n,\psi}(q_n) \end{bmatrix}. \tag{3.52}$$

$a_{x,\psi}$ is a vector containing the distances an X-ray beam travels through each orientation region in the sample:

$$a_{x,\psi} = \begin{bmatrix} a_{\phi_1,x,\psi} \\ a_{\phi_2,x,\psi} \\ \vdots \\ a_{\phi_n,x,\psi} \end{bmatrix}. \tag{3.53}$$

Each coefficient in $a_{x,\psi}$ will then be the line integral along a line l, following the X-ray beam, of a function which is one if the region in the sample has orientation ϕ_m, and zero if it has not. This can be formalized mathematically as

$$a_{\phi_m,x,\psi} = \int_l f_m(s,t)dl' \begin{cases} f_m(s,t) = 1 & \text{if } \phi(s,t) = \phi_m \\ f_m(s,t) = 0 & \text{if } \phi(s,t) \neq \phi_m \end{cases} \tag{3.54}$$

where the function $\phi(s,t)$ is the orientation distribution across the sample. By selecting all $a_{\phi_m,x,\psi}$ for all x and ψ, the sinograms of the radon functions for each f_m are created. It is then possible to do a standard filtered Fourier backprojection to get the function $f_m(s,t)$. Finding all f_m will give the orientation distribution $\phi(s,t)$.

Solving the Linear Set of Equations

To find the distances the X-ray beam travels through each region, in each projection, Equation 3.50 needs to be solved. The scattering matrix S_ψ and the intensity on the detector $I(\mathbf{q})_{x,\psi}$ are known. For a "perfect" experiment, it would only be needed to take the inverse of the scattering matrix to find the vector $a_{x,\psi}$:

$$a_{x,\psi} = S_\psi^{-1} I(\mathbf{q})_{x,\psi}. \tag{3.55}$$

There are however no such things as a perfect experiment since it will always be noise from background radiation and other scatterers in the sample. In addition the theoretical model for the scattering is not a perfect model for how the particles scatters. Because of this; solving for $a_{x,\psi}$ by using Equation 3.55 could give completely different coefficients in $a_{x,\psi}$ than the real ones.

It was therefore chosen to minimize the function

$$f(a_{x,\psi}) = (S_\psi \cdot a - I_{x,\psi})^2 = a_{x,\psi}^{\mathrm{T}} S_\psi^{\mathrm{T}} S_\psi a_{x,\psi} - 2 I_{x,\psi}^{\mathrm{T}} S_\psi a_{x,\psi} + I_{x,\psi}^{\mathrm{T}} I_{x,\psi}, \tag{3.56}$$

under the constraints that all coefficients in $a_{x,\psi}$ should be positive, and the sum of them should be equal to the total distance the X-ray beam travels through the sample for the given projection and angle in the tomography scan. This kind of optimization problem is known as *quadratic programming*. Several methods exist for solving such problems, and quadratic programming has been thoroughly covered in literature. To give a good description of how to solve such problems would be a lengthy affair, as it also would be needed to describe problems as degeneracy. This is not seen as relevant for this thesis, as it is not essential to the problem discussed. In addition, many so-called "black box"-scripts have been written and thoroughly tested by thousands of people, making it both unnecessary and unwise to create own code to solve such problems. To solve the problem of fitting the theoretical scattering pattern to the experimental one the function *quadprog()* in `Matlab` was used.

In short, solving a quadratic programming problem is done by taking the Lagrangian of the function to be optimized and, depending on the algorithm used, recursively solve for the unknown variables in the problem. Further information can be found in [25, 26].

Chapter 4

Procedure

4.1 Experimental Set Up

The experimental measurement included in this thesis were carried out at the cSAXS beam line at the Swiss Light Source (SLS) at the Paul Scherrer Institute in Switzerland. The SLS is a third generation synchrotron, and the cSAXS beamline is specialized for coherent small-angle X-ray scattering. The set up in front of the sample can be seen in Figure 4.1 The diamond filter is used to separate the vacuum of the synchrotron and the beam line and the beam position monitor is used for aligning. The slits control the shape of the beam. The monochromator works by only letting those wavelengths which can fulfill the diffraction condition of the (111) reflection in a

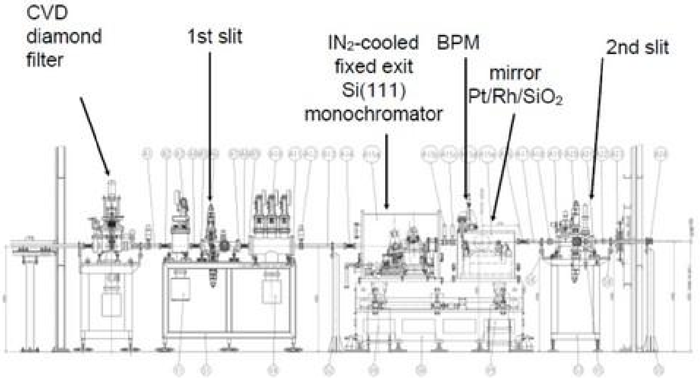

Figure 4.1: The optics before the X-ray hits the sample. Figure adapted from the SLS website[1].

---

[1] The figure can also be found at http://www.psi.ch/sls/csaxs/beamline-layout

Si-crystal through. By changing the angle of the crystal compared to the X-ray beam, different wavelengths can be chosen. The mirror filters out higher harmonics in the diffracted wave from the silicon crystal, making the beam monochromatic. This works by having the mirror very close to the critical angle. The critical angle is proportional to the wavelength of the X-ray beam [21]. X-rays with low wavelengths will therefore be totally reflected, while X-rays with higher wavelengths will be refracted into the mirror. The the set up after the optics is shown in Figure 4.2. The sample itself was placed on various piezoelectric translation and rotation stages and placed so that the X-rays hit the neck of the dog bone. After the sample the X-rays went through a 7 m long flight tube before hitting the detector.

Figure 4.2: The experimental set up after the X-ray optics in Figure 4.1. i: X-ray optics, ii: sample, iii: flight tube, iv: beam stop, v: Pilatus 2M detector.

4.2 Analysis of the Experimental Data

4.2.1 Fitting Theoretical Scattering

To fit the theoretical scattering to the experimental data, the form factor was calculated for various shapes. This was then convoluted with a Gaussian function to accommodate for both polydispersity and the fact that the detector has finite resolution. Since (in practice) all photons hitting a pixel will be registered at the same q-value, each pixel gives the integrated intensity over the region the pixel covers. The parameters giving the best fit was chosen to be used in the further analysis.

After the general shape of the theoretical scattering signal was fitted to the experiment, the experimental data were corrected for absorption, as described in Equation 3.45. The absorption in the iPP sample was not precisely known. It was also impossible to use the voltage from the diode placed as a beam stop to estimate the attenuation coefficient, because part of the SAXS signal hit this diode. This influenced the apparent absorption because the SAXS signal from the talc particles depended on their orientation. An absorption coefficient was used in the correction which made the experimental data fit with the theoretical data for two distinct cases. One case where the beam only traveled through a region where the talc particles had their surface normal oriented perpendicular to the X-ray beam, and one case where the beam only traveled through a region where the talc particles had their surface normal oriented parallel to the X-ray beam. The attenuation coefficient used was $\mu = 2.85\ \text{cm}^{-1}$. This attenuation coefficient seems to be in agreement with theory, and will be discussed in Section 6.1.

4.2.2 Creating Experimental Tomograms

The data recorded by the detector was sectioned into 16 different sectors, where all the data along one radial line in the detector was averaged to form a one dimensional scattering pattern, $I(q)$, in each sector. How these sectors built up the detector can be seen in Figure 4.3.

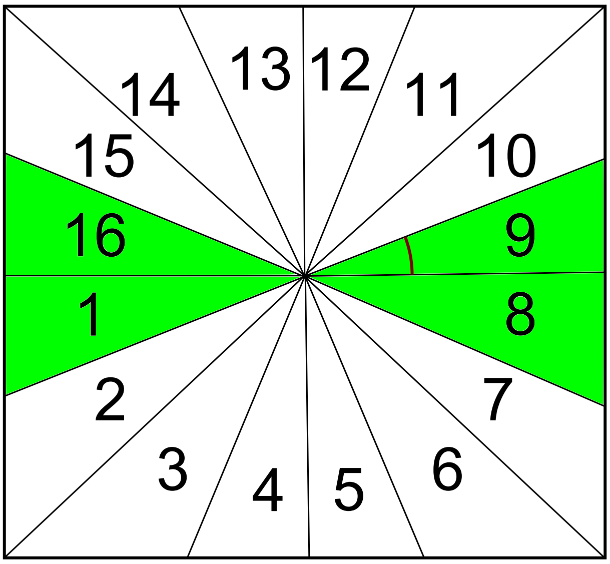

Figure 4.3: How the detector screen was sectioned into 16 different sectors. The green sections are the regions containing the "horizontal scattering". The dark red circle segment is the radial line where the intensity is integrated up and averaged by the number of pixels along the radial line, which makes each sector a one dimensional representation of the scattering pattern.

Two tomograms were constructed from the experimental data. One was created using the voltage of the diode placed as beam stop, and would then ideally give information on the attenuation coefficient in the sample. This was done to see the shape and orientation of the sample itself and could be compared to later tomograms based on the scattering pattern to verify if the reconstructed image behaved as expected. The second tomogram was created by summing up the entire horizontal scattering pattern, cf. Figure 4.3, after correcting for attenuation in the sample. This would make it possible to compare later simulations, where the scattering in the tomography scan was simulated and then reconstructed.

4.3 Simulating Tomography Scan Procedure

To see if the model used would be a good approximation to the real scattering from a talc particle, a simulation of the scattering in the tomography scan was performed. The talc particles were modeled as an oblate ellipsoid where the x'- and z'-radius are equal and 1.25 µm and the y'-radius is 0.5 µm. The talc particles thus look like disks, and a sketch can be seen in Figure 4.4. It is known that the talc particles align themselves with their y'-axis parallel to the outer edge surface normals [5]. For illustrative purposes it will be assumed that the sample consisted of only four different regions, where the

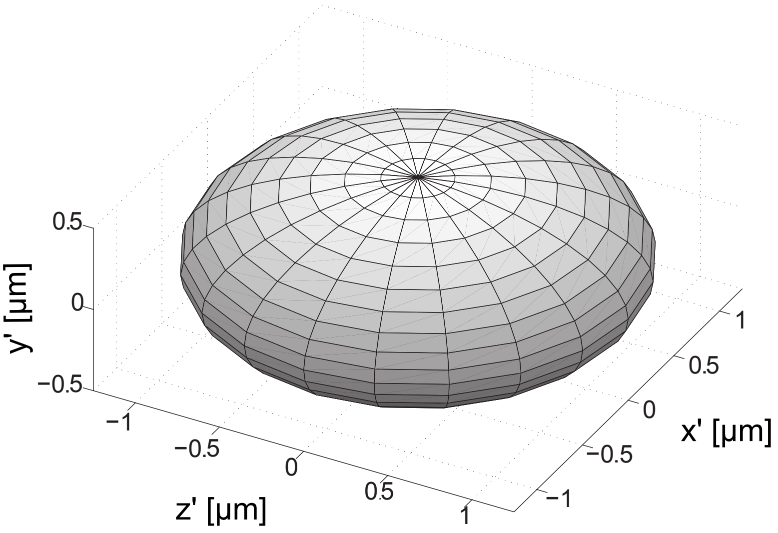

Figure 4.4: A sketch of one talc particle.

talc particle was either pointing horizontal or vertical, seen in Figure 4.5. To see how the particle orientation affected the tomograms, it was necessary

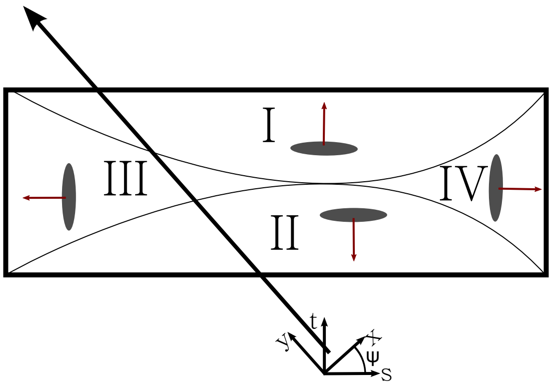

Figure 4.5: How the talc particles, grey disks, were oriented in the simulation. The change in direction for this example is abrupt, and not continuous as in the real sample. The long black arrow symbolizes an X-ray beam traveling through the sample when the sample is oriented at ψ degrees compared to the laboratory frame.

to model the scattering in the horizontal direction. Equation 3.18 says that the scattering intensity is proportional with the absolute square of the form factor. The tomographic scan was simulated by taking a line scan at different positions, x, through the sample and measuring what distance through the sample the X-ray beam traveled through regions I and II, and III and IV, as can be seen in Figure 4.5. The SAXS pattern was then simulated by taking the distance through I and II and multiplying it with the absolute square of the form factor for the particles, for a $\mathbf{q}$-vector in the horizontal direction, and adding the distance through area III and IV multiplied with the absolute square of the form factor for a horizontal $\mathbf{q}$-vector, as described in Equation 3.49. In practice this calculation was done by creating n different matrices, where n now is a whole number, for all the different orientation regions representing f_m in Equation 3.54. These matrices had the value one if the initial orientation at that position was ϕ_n and zero otherwise. Then the radon transform was performed on each different matrix for different angles and multiplied by what the scattering intensity would be for talc particles with that orientation to get the scattering signal from each region. These n scattering signals for each projection were then summed up to give a model for the entire scattering signal. Figure 4.6 shows four different regions with different initial orientation ϕ_m for a model of the sample where $n = 36$.

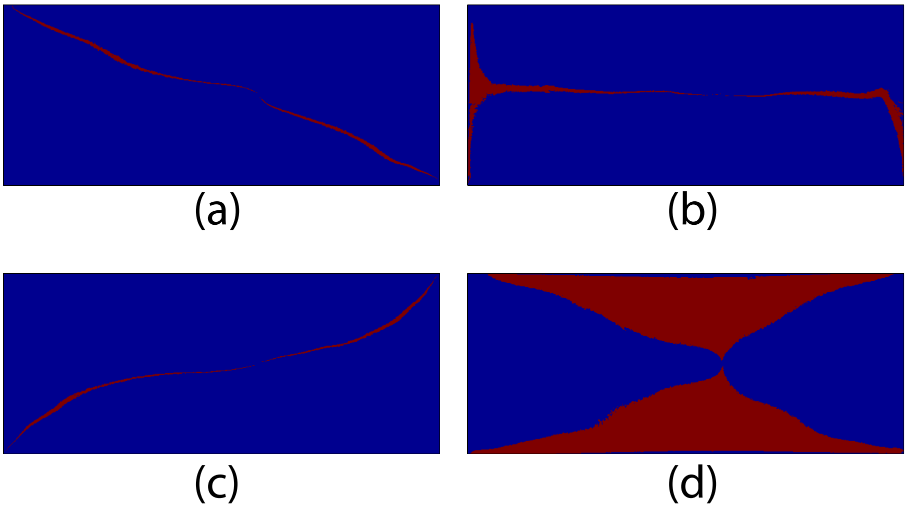

Figure 4.6: Different matrices with different initial orientation ϕ_m. Red means that region has talc particles with the orientation ϕ_m, while blue color means the particles have another orientation. The regions shown have the orientation (a) -45°, (b) 0°, (c) 45° and (d) 90°.

The particle density was approximated to be equal throughout the sample, which means the factor n in Equation 3.47 is a constant and can be normalized out of the equation. These SAXS patterns were calculated for multiple projections through the sample, which means that the black arrow in Figure 4.5 would be moved in the x-direction, and for angles, ψ, in the interval $[0, 180\rangle$. The numerical values for the scattering vector were similar to those in the experimental data acquired at the cSAXS beam line, namely $q = 0.038\ \text{nm}^{-1} - 0.425\ \text{nm}^{-1}$. These values for the q-range was set to be sure the non-circularly shaped beam stop would affect the measurements, and because the scattering signal seemed to be significantly influenced by scattering from other kind of particles in the sample for q-values larger than $0.425\ \text{nm}^{-1}$. The SAXS patterns were integrated up and the filtered Fourier backprojection was computed in a similar way as done for the experimental data.

4.4 Retrieving Orientation Distribution by Simulated Annealing

An idea for reconstructing the orientation distribution of the talc particles in the iPP sample was to construct an energy function, and try to minimize this by the use of the numerical method *Simulated Annealing*. This was done by making an initial guess of the orientation distribution, as can be seen in Figure 4.7, and then simulating a tomography scan as outlined in Section 4.3. This initial guess was taken because it was known prior to the start of the simulation to resemble the true orientation, and should therefore be a good starting point to see if the algorithm works. The sinogram to the initial configuration was then compared to the sinogram of the simulated SAXS tomography scan of the true talc orientation distribution, as can be seen in Figure 2.4. The function, E, to be minimized was then defined as

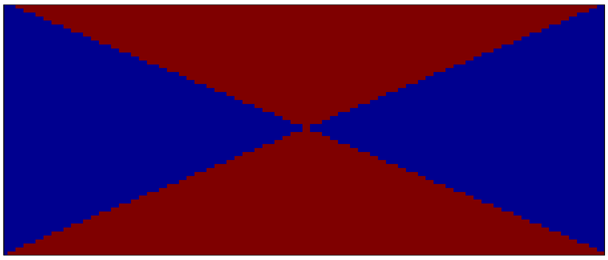

Figure 4.7: The initial guess of the orientation distribution. Blue areas: talc particles with their surface normal horizontal, red areas: talc particles with their surface normal in the vertical direction.

$$E = \sum_{i,j} \left(S_s(i,j) - S_t(i,j)\right)^2 , \tag{4.1}$$

where S_s is the sinogram of the SAXS tomography scan with the current orientation distribution, while S_t is the true sinogram. S_t would eventually be the experimental data, but is now only a chosen correct sinogram from the simulation of the horizontal scattering in the tomography scan.

With the function to be minimized in Equation 4.1 and the initial guess of the orientation in Figure 4.7, the initial T parameter, T_0, in Equation 3.48 and the factor it should decrease with after each cycle, δT, had to be set. Finding the optimal values for these parameters is often dependent on how the system behaves, and what kind of function is to be minimized. These values often have to be found by trial and error [24]. The parameter values used, the number of Monte Carlo steps in each cycle and the number of cycles performed can be found in Table 4.1. These were chosen based on the time required to run each configurations and the and that the initial value of the function which was to be minimized was i the order of 10^2. It should be noted that the model representing the iPP sample was 63×151 pixels large.

Table 4.1: Different parameters used in the simulated annealing method

Configuration #	T_0	δT	MC steps	Cycles
1	400	0.65	20 000	15
2	600	0.65	20 000	15
3	600	0.75	20 000	15
4	800	0.80	20 000	15
5	1200	0.55	20 000	15

4.5 Retrieving Orientation Distribution by a Linear Set of Equations

Equation 3.56 was minimized to find the distances the X-ray beam traveled through the different regions in the sample. One of the constraints in this fitting was that the sum of all the distances the X-ray beam traveled through the different orientation regions inside the sample should be equal to the total distance the X-ray beam travels through the entire sample. This would be the distance from where the X-ray beam enters the sample, to where it exits. To find the distance the X-ray beam traveled through the sample for each projection and for each angle in the tomography scan, the radon transform of a function with the exact same shape and dimensions as the true sample, and with value one if it was inside the sample and zero if it was outside, was performed so that each projection would be proportional with the distance from where the X-ray beam enters the sample to where it exits. This function is visualized in Figure 4.8. These radon transforms were compared to the sinogram of the experimental scattering data, as seen in Figure 4.9. The two black and green rings marks where the X-ray beam first hits the sample for two different angles ψ in the tomography scan. These are placed at the exact same projection and scan angle, showing that the radon transform of the sample shape is properly aligned with the experimental data.

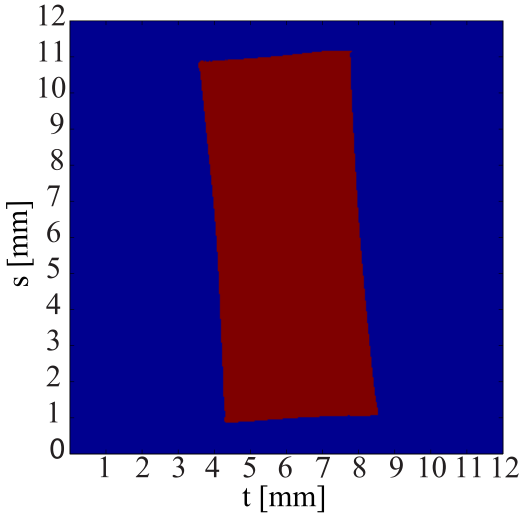

Figure 4.8: The figure shows a region with the exact same shape as the true iPP sample. The red color is marking the sample, while the blue color is marking air. The s- and t-axis is not perfectly aligned with the sample, as they have been presented earlier, but is representing them according to how they were in the experimental set up.

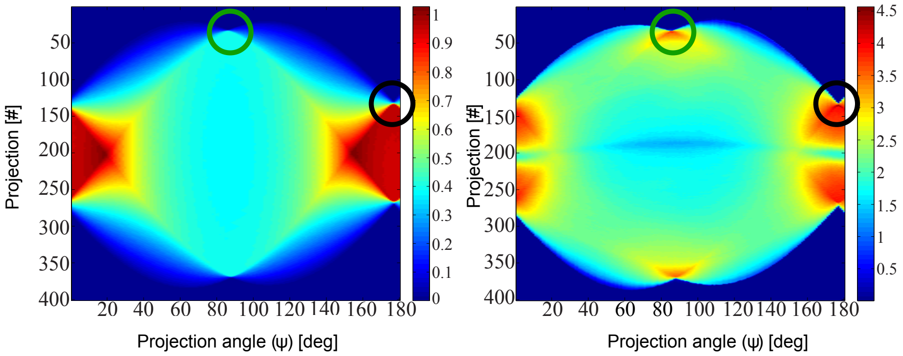

Figure 4.9: (a) The radon transforms of the distances an X-ray beam travels through a shape with same dimensions as the true iPP sample. The color gives the distances in cm. (b) Total recorded intensity of the scattering from the iPP sample in the tomography scan. Number of counts are on a logarithmic scale. The black and green rings in figure (a) and (b) show where the X-ray beam first enters the sample for the incoming beam parallel to the short and long sides of the sample, respectively.

Chapter 5

Results

5.1 Experimental Scattering Data

Two figures of the 2D scattering pattern are shown in Figure 5.1 (a) and (b). These are both taken directly from the detector, with no sort of correction or altering applied to the data. Although only the horizontal part of the scattering signal was used, these figures are added to make it easier for the reader to follow the discussion when it is referred to the horizontal scattering. The two scattering patters are representative for how all the different 2D scattering patterns looked, and show two typical scattering experiments. One where the X-ray beam travels through the iPP sample where all the talc particles have the same orientation, Fig. 5.1 (a), and one where the X-ray beam travels through the iPP sample where the talc particles have multiple different orientations, Fig. 5.1 (b).

5.2 Tomograms of Experimental Data

Figure 5.2 shows the tomogram based on the diode signal. By this reconstruction it would look like the attenuation coefficient is higher towards the edges, than in the middle of the sample. Unfortunately, the low-q part of the SAXS signal hits the beam stop, and depending on what sample regions the X-ray beam travels through this will modify the signal. The marked attenuation coefficient is therefore not the correct, but it is reassuring that it is in the correct order of magnitude. This tomogram gives a very clear representation of the shape and external orientation of the sample in the experimental set up.

The tomogram based on the horizontal scattering pattern is shown in Figure

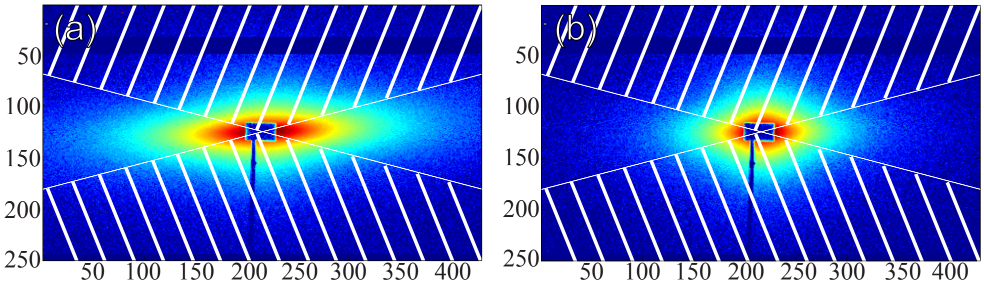

Figure 5.1: Experimental 2D scattering patterns from the SAXS measurements. (a) is the scattering pattern where the X-ray beam has traveled through the iPP sample where all the talc particles have the same direction. (b) shows the scattering pattern where the X-ray beam has traveled through the iPP sample where the talc particles have a number of different orientations. The unshaded area between the white lines is the part of the scattering pattern which is referred to as the horizontal scattering signal. The rectangular beam stop at the center contained a diode. Axis indicate pixel number on detector

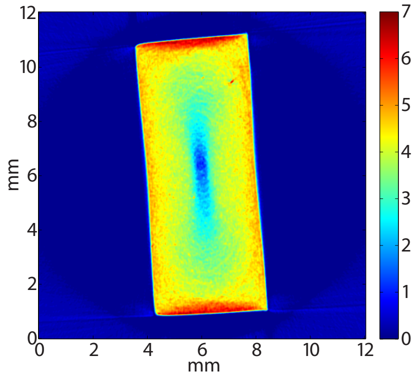

Figure 5.2: A tomogram based on the voltage readout from the diode used as beam stop in the experimental set up. This would represent the attenuation coefficient in the sample, in units 1/cm. It seems like the attenuation coefficient is higher towards the edges of the sample, compared towards the center. The external shape and size of the sample is well defined by this tomogram.

5.3. Here the sum of all counts of the detector pixels in the horizontal direction has been made after correcting for absorption according to Equation 3.46. By reconstructing it in this way, one can clearly recognize the size and shape of the iPP sample, although the value in the tomogram itself does not have any direct physical meaning or units.

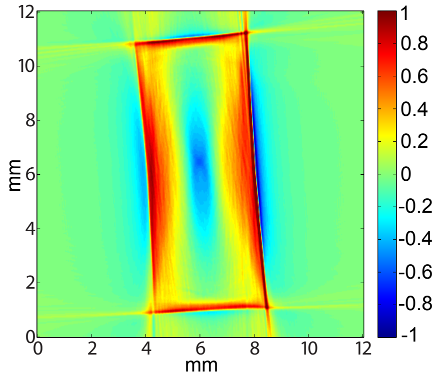

Figure 5.3: A tomogram based on the entire horizontal scattering pattern from the iPP sample. The image intensity values have no obvious physical meaning, and has hence been normalized to 1. Some artifacts are shown at the corners of the sample, showing a few lines in the vertical and horizontal direction. The general tendency is that the value in the tomogram is negative at the center, and growing towards positive values towards the edges.

5.3 Fitting Theoretical Scattering

As it is crucial to have a good approximation of the theoretical scattering pattern to the experimental, several different sizes and shapes where tested to get the best fit. Figure 5.4 shows the best fit of the scattering vector when the form of the particle is shaped as a spheroid, for the case where the scattering vector lays in the $x'z'$-plane, and one case where the scattering vector is in the y'-direction. How these scattering vectors are oriented compared to the shape of the particle can be seen in Figure 4.4. The spheroid which gave the results in Figure 5.4 had average dimensions: diameter $d = 2.5$ µm and height $h = 1$ µm. This height, or thickness, of the talc particles is the same as the SEM pictures in Figure 2.5 indicates, but the diameter could be argued to be a little too small compared to the observed talc particles in Figure 2.5, where there is a lot of particles with diameter in the range between 5-10 µm.

The results of trying to fit the experimental data with theoretical scattering from a particle shaped as a cylinder is shown in Figure 5.5. These fittings show that it is not possible to fit both the scattering in $x'z'$-plane and the scattering in the y'-direction at the same time. Changing the radius and

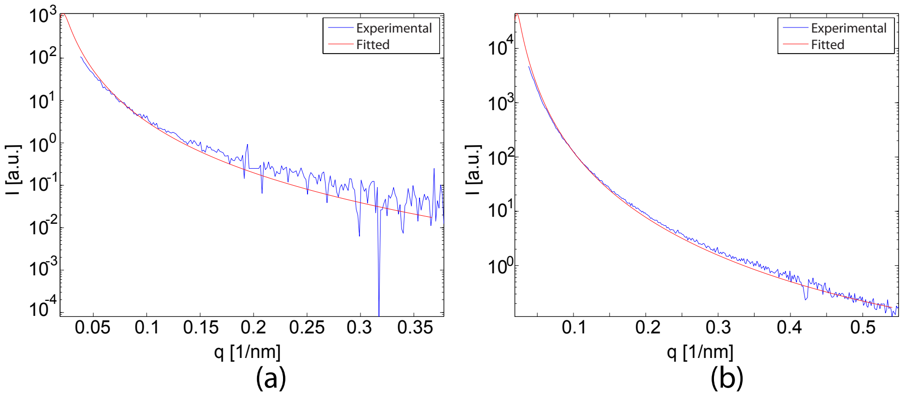

Figure 5.4: The red curves are fitted theoretical scattering from a spheroid to the blue experimental data for the cases where the scattering vector is in the $x'z'$-plane, (a), and y'-direction, (b). After a background of 0.07 has been subtracted from the data it is rather good agreement between the two curves. The intensity is measured in arbitrary units. The sharp drop in figure (a) at $q = 0.32$ nm^{-1} is most likely caused by some defects in the detector.

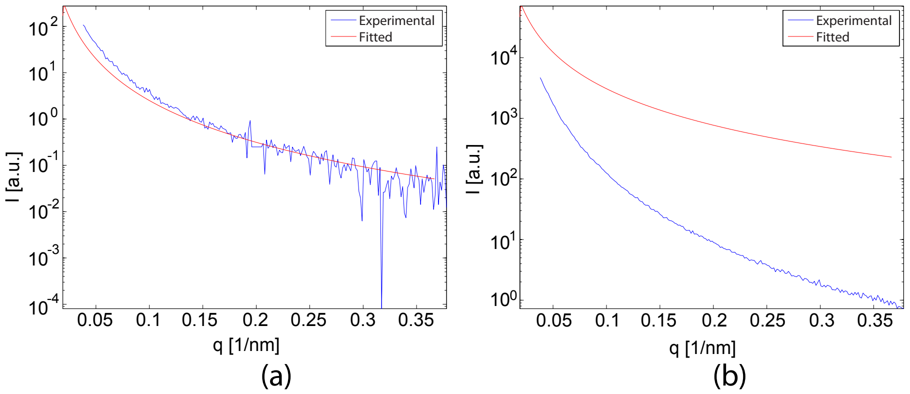

Figure 5.5: The red curves are theoretical scattering from a cylinder shaped particle fitted with the blue experimental data. (a) is scattering in the $x'z'$-plane, which is the circular plane of the cylinder, and (b) is in the y'-direction. A background of 0.07 has been subtracted from the experimental data and the intensity is in arbitrary units.

height of the particle did not give any significant improvement in the theoretical scattering compared to the experimental. To emphasize the problem with the cylinder model, Figure 5.6 shows how the theoretical scattering in Figure 5.5(b) looks compared to the experimental when the theoretical scattering is normalized to the intensity of the experimental data. It is clear that the absolute square of the form factor does not fall off quick enough to fit the experimental data.

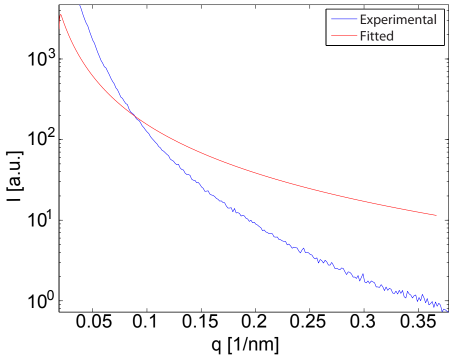

Figure 5.6: The theoretical curve for scattering from a cylinder in the $q_{y'}$ direction, which is through the flat top part, drops down much slower than the experimental data.

From these results it is clear that the spheroidal shape is a far better model than the cylindrical one for modeling the shape of the talc particles. The random fluctuations also seem to contribute rather much at high scattering vectors compared to the signal itself. This is especially evident i Figure 5.4 (a).

5.4 Simulated Tomography-Scan of iPP

The reconstructed tomogram based on a simulated tomographic scan, as described in Section 4.3, is shown in Figure 5.7 (a), and can be compared to the tomogram reconstructed by the use of experimental data in Figure 5.7 (b). The simulated tomography scan was done by accounting for polydispersity of the particles, and letting all the talc particles in the sample have one out of 36 different orientations. The main features are the same in both tomograms, with an area along the edges with high values, and a negative value in the center, which strengthens the hypotheses used in this thesis. It is however not perfect agreement, which means that the model can be improved in some way. The simplification of not accounting for low counting statistics for high q and not considering other scatterers in the sample could be two of the reasons why they are not in perfect agreement. The fact that the talc particles are not perfect spheroids also cause differences.

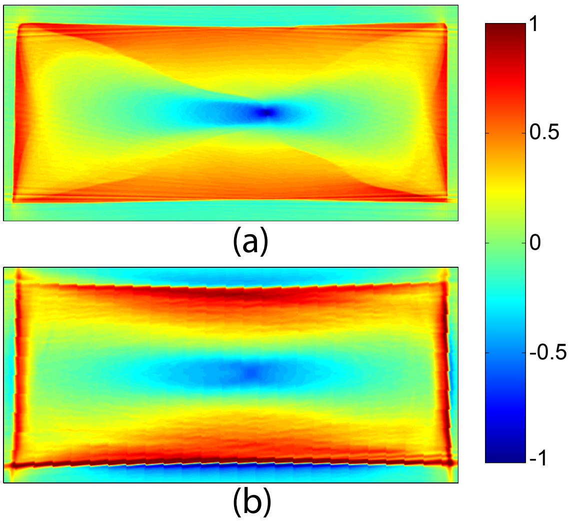

Figure 5.7: Two tomograms based on the (a) simulated and (b) experimental horizontal scattering from an iPP sample. since the value that comes out of the reconstruction has no clear physical meaning the data have been normalized to emphasize the similarities and the color scale is to help the reader know what color is high and low. A general similarity between the simulated and experimental tomogram can be seen. The area along the edges has a high value, while the center has a negative value for both tomograms.

5.5 Reconstruction of Orientation

5.5.1 Reconstruction Based on Simulated Annealing

The results of trying to reconstruct the orientation distribution with simulated annealing is shown in Figure 5.8. This figure shows the results for all the five different configurations shown in Table 4.1.

Figure 5.8 (b)-(e) are identical, which means that varying the T_0 and δT parameter had little effect. It also shows little resemblance with the true orientation distribution, as seen in Figure 2.4. It is apparent that the algorithm used didn't manage to retrieve the orientation distribution even when using simulated data from perfect monodispersive scatterers and with no noise in the scattering signal. The number of regions tried to retrieve was $n = 36$.

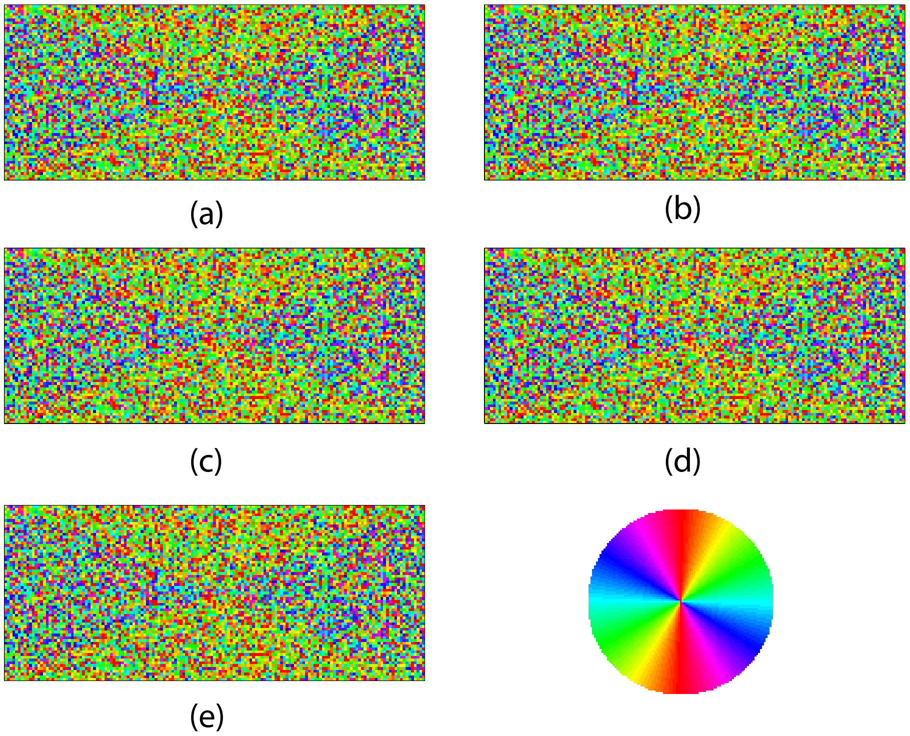
(a)
(b)
(c)
(d)
(e)

Figure 5.8: The orientation distribution reconstructed by simulated annealing. (a) - (e) represent configuration 1-5 in Table 4.1. The colors give the direction of the talc particles surface normal, indicated by the color wheel inset.

5.5.2 Reconstruction Based on Linear Set of Equations

When reconstructing the orientation distribution by using a linear set of equations, several steps towards the full retrieval of the orientation distribution were done, from perfectly monodisperse particles, to more complex scattering where different sized particles scatter. These steps are all presented in this section to emphasize how increasing complexity alter the reconstructed orientation distribution.

Reconstructing the Orientation Distribution from Synthetic Datasets

The horizontal scattering patterns obtained from simulations of monodispersive talc particles were used to retrieve the original orientation distribution in the sample by the method described in Section 3.8.1. The result of this reconstruction can be seen in Figure 5.9. There are some artifacts at the boundary between regions, where the orientation in general is higher than

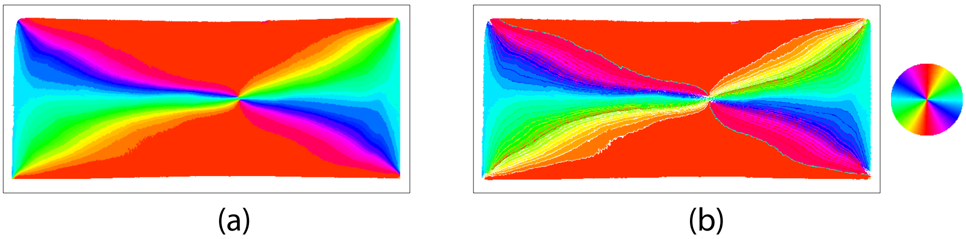

(a) (b)

Figure 5.9: Reconstructing orientation distribution of a synthetic dataset. (a) The model of the orientation to the talc particles in the sample with 36 different regions. (b) The reconstructed orientation of the talc particles surface normal based on the syntesized horizontal scattering test patterns. The orientation is indicated by the color wheel inset.

it should be, but besides that the reconstruction works very well. This reconstruction of the simulated sample works well in determining the different regions where the orientation is different. It is however emphasized that this is by the use of simulated data, with particles of shape as spheroids of a single size and very high detector resolution with no noise.

Reconstructing from Polydisperse Particles

Retrieving the orientation distribution from simulated horizontal scattering patterns, where also polydisperse and finite detector resolution are taken into account, is shown in Figure 5.10. This reconstruction clearly shows that with

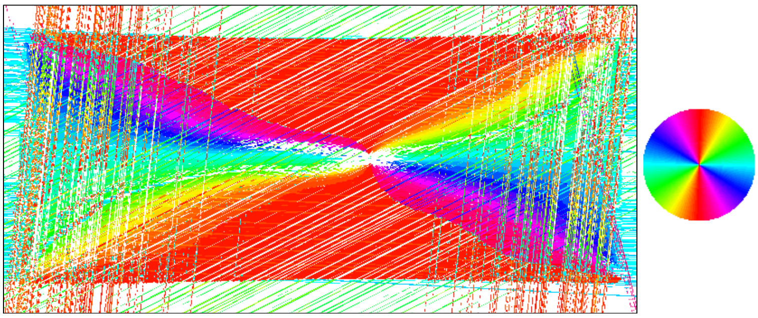

Figure 5.10: The reconstructed orientation distribution from simulated scattering patterns, where polydispersity is taken into account, shows the original distribution. The streak artifacts are caused by polydisperse particles and finite detector resolution.

the smoothening of the scattering patterns, arising because of polydispersity, it creates more artifacts when retrieving the original orientation distribution.

Sinogram of Distances Through Regions

Figure 5.11 shows a typical sinogram of the distances the X-ray beam travels through a certain region with talc orientation ϕ in the experimental tomography scan. We have chosen to only show one of the sinograms for these radon transforms since they all show the same tendencies. The rest of the sinograms can be found in Appendix A. It can be seen that the sum of all distances in one projection angle is not equal between the different projection angles. This is especially evident between $\psi = 61°$ and $\psi = 65°$ where the X-ray beam according to the reconstruction does not travel through this given region at all.

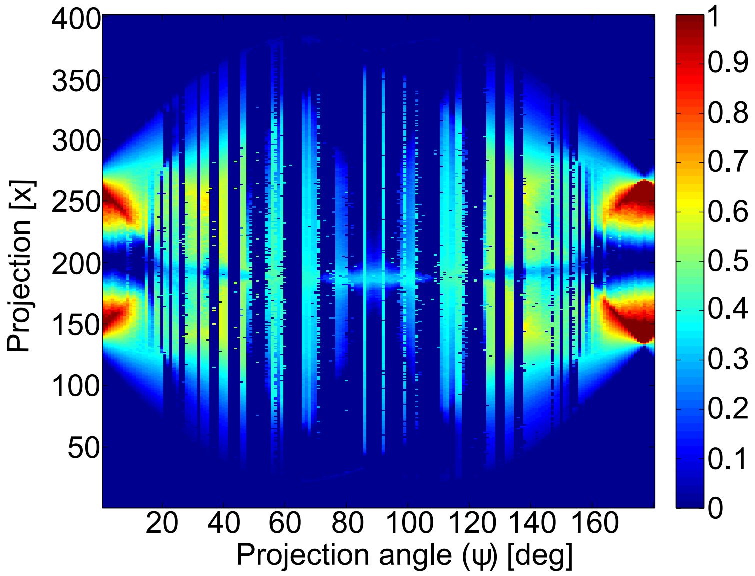

Figure 5.11: The figure shows the radon transforms of the distance the X-ray beam travels through a region in the iPP sample where the orientation is ϕ. The color indicates the distance, in units of cm, the X-ray beam traveled through the region for each projection as given by the colorbar.

Reconstructing a Bimodal Orientation Distribution from Experimental Data

To retrieve the orientation distribution of the talc particles in the real iPP sample, by using the experimental data, it was assumed that the sample would only contain talc particles with two different orthogonal orientations. The result from this reconstruction can be seen in Figure 5.12. By comparing it with Figure 2.4, which is the true orientation distribution of the talc particles, it is seen that the main features agree well between the figures. It is clear that the flake normals are aligning themselves parallel with the external surface normals of the sample.

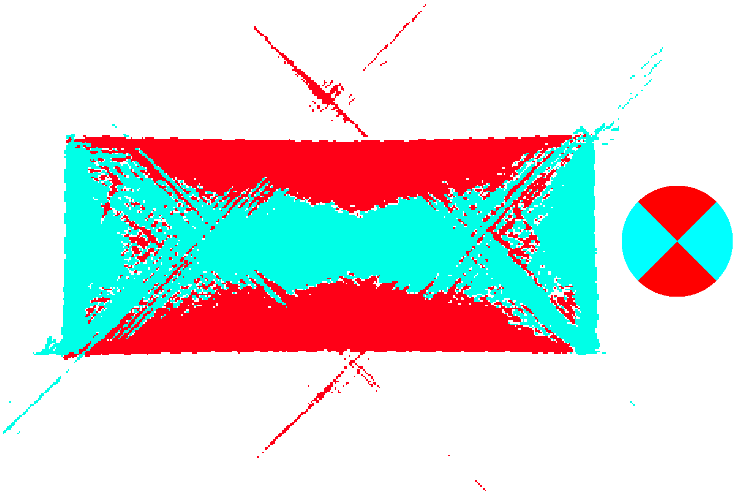

Figure 5.12: The figure shows the retrieved orientation distribution by using experimental data. The color indicates the direction of the talc particles surface normal as given by the color wheel inset. The red cross above and below the sample are artifacts due to imperfect datasets.

Reconstructing 4-modal Orientation Distribution from Experimental Data

Reconstructing a 4-modal orientation distribution is shown in Figure 5.13. It is still possible to recognize the main features of the true orientation distribution seen in Figure 2.4, although more artifacts appear than for the tomogram reconstructed with fewer orientation regions. There are for instance regions inside the sample with no specified orientation, marked with white color, which is a sign that the reconstruction algorithm fails for these areas because of incorrect radon transforms of the distances $a_{\phi_i,x,\psi}$. The red and light blue regions are located at the same position as in the true orientation distribution, while the purple area has direction from top left towards bottom right, and the green area has direction from bottom left towards upper right, as they should according to the real orientation distribution.

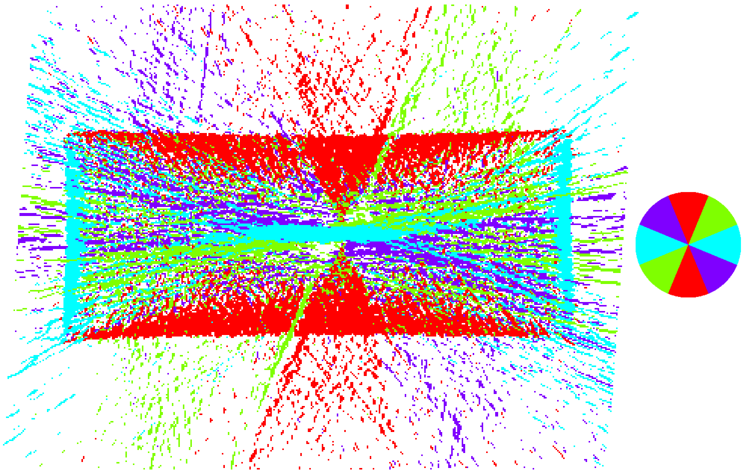

Figure 5.13: A reconstruction of four regions with different orientation in the iPP sample. The colors indicate the direction of the talc flakes surface normal, given by the color wheel inset. There are many artifacts caused by the difficulty of fitting the experimental parameters to theoretical ones. Various regions in the interior of the sample also have no specified orientation, marked with white color.

Reconstructing 6-modal Orientation Distribution from Experimental Data

Increasing the number of distinct regions of uniform orientation reconstructed to six is shown in Figure 5.14. The different orientations of the talc particles are given by the color wheel. This tomogram looks quite messy at first glance, with a lot of artifacts. It is however still possible to recognize the red and light blue region when comparing it with Figure 2.4. The pink region looks to have a tendency of laying above the dark blue region in the left part of the tomogram, and below in the right part, as it should according to the real orientation distribution. The yellow region can be argued be below the green region in the left part of the tomogram, and above in the right part, also this as it should, but this is most likely only possible to see because it is known to be that way from earlier experiments. The green and dark blue regions are almost non existent. It is also apparent that the borders between the different regions are very diffuse. An important remark about this reconstruction is that the resolution of the orientation distribution of the talc particles is higher than what should be possible based on the segmentation of the detector, as will be discussed in Section 6.3.2. It was still chosen to add this attempt to reconstruct the orientation distribution for six regions to see what the effect would be when this resolution limit was violated.

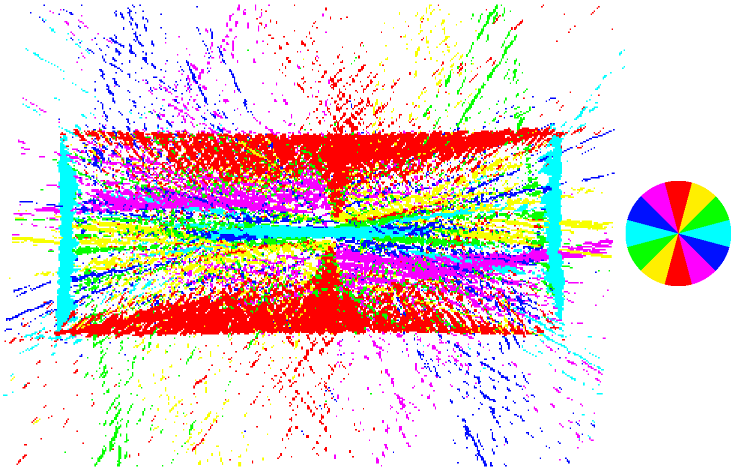

Figure 5.14: The figure shows the orientation distribution of talc particles in the iPP sample. Six different regions have been reconstructed and the color indicates the direction of the talc particles surface normal, as given by the color wheel inset. There is a lot of artifacts outside the sample, and the regions inside the sample are therefore unlikely to be very precise.

Chapter 6

Discussion

6.1 Absorption Corrections

The absorption coefficient in the iPP sample was set to $\mu = 2.85$ cm^{-1} in order to fit the experimental data to the theoretical ones. This is between the value of the absorption coefficients for talc and polypropylene, which are 23.1 cm^{-1} and 0.94 cm^{-1}, respectively. It should be expected that the attenuation coefficient is closer to polypropylene than talc, since the volume percent of polypropylene is higher in the sample than talc. The attenuation coefficient was measured by fitting experimental data, rather than directly measuring it. This creates more uncertainty about the model used for the scattering. If the attenuation coefficient had been measured precisely it is one less unknown variable of the total system, and this would have made it easier to alter the scattering model to a more correct one.

6.2 Fitting Experimental Data

By trying to fit the theoretical model of the form factor to the experimental scattering data, it is clear that approximating the particles as oblate spheres is far superior to approximating the particles as cylinders. This is apparent when comparing Figure 5.4, 5.5 and 5.6. It was not possible to fit the experimental scattering to the cylinder model for scattering in both the $x'z'$-plane and the y'-direction using the same normalization constants for both directions. The magnitude of the scattering intensity in $q_{y'}$ was much stronger in the theoretical model than for the experimental data. It was also apparent that when trying to normalize the theoretical data in $q_{y'}$ to fit with the experimental data, the shape of the curve was not correct for the theoretical case. The theoretical curve decreased at a slower rate.

The full spheroid model, on the other hand, worked much better. Here it was possible to fit the shape and intensity of the experimental data for both the $q_{x'}$ and $q_{y'}$ direction using the same scaling parameters. The fit also looks quite good, and should imply that the full spheroid model is an accurate model to use.

Figure 5.4 (a) still implies some problems with the experiment performed. For scattering in the $q_{x'}$ direction it can be concluded that the counting statistics for heigh q-values are too low. This means that those intensities cannot be used to fit the theoretical data, because they are too much influenced by noise. Since only low q-values can be used for fitting the theoretical scattering to the experimental, this can make it difficult to find the distances, $\{a_{\phi_i,x,\psi}\}$, the X-ray beam travels through the different regions. Particles differing in orientation by only a small angle will have almost identical form factor when comparing the scattering amplitudes for low q-values. The scattering matrix S used for finding the distances will then be close to singular. It can then be expected that the reconstructed tomogram will have a large number of artifacts when trying to retrieve different orientations, because the algorithm will have problems separating two regions where the angle between the different oriented talc particles is small.

To get a good fit between the theoretical data and the experimental data, a background intensity of 0.07 a.u. was used up to $q = 0.43$ nm^{-1}. This is likely caused by other scatterers in the sample and background radiation. Since this scattering from other particles most likely is not constant for different q-values, the background intensity should also fall off at higher q. Because the counting statistics were rather low for high q, it was not attempted to try to find this precise background intensity, because the intensity at high q would anyway be too uncertain to use in the fitting routine,. Therefore only q-values up to $q = 0.43$ nm^{-1} were used.

The optimal "average" height and diameter of the spheroid used for fitting the theoretical scattering intensity to the experimental were found to be 1.0 µm and 2.5 µm. The hight of the particles is close to what is observed in the SEM-pictures, in Figure 2.5, but the diameter appears to be too small. It is not clear what the cause of this could be, but it is certain that the material causing scattering is the talc particles rather than polypropylene crystallites. At the same time as the data used in this thesis was measured, scattering on a sample of polypropylene without talc was performed. This sample showed much less scattering intensity, making it certain that it is the talc particle scattering that dominates. This is further evidenced by the fact that the orientation of the SAXS signal, seen in Figure 2.4(b), when performing a raster-scan of a physically cut cross section is in full agreement with WAXS measurements performed earlier, seen in Figure 2.4(a). It should therefore be without doubt that what is causing the scattering for low q in the sample is the talc particles. When looking at the SEM-pictures of the talc particles, the diameter of the particles looks to be in the range of 5-10 µm. Although there are many large particles, there are also many small particles, with diameter below 5 µm. One reason why the ratio between the average height and diameter of the talc particles looks to be different in the theoretical model of the particles and in the SEM-pictures could be caused by the finite size of the X-ray beam. The width and height of the focused X-ray beam was approximately 20×20 µm^2. This is close to the diameter of the largest particles, and it is likely that the largest particles are only partly illuminated by the beam for each step interval in the tomographic scan. It would be impossible to get signal from the entire shape of the particle if parts of it is outside the beam. Only parts of the talc particles would give rise to any signal, which is illustrated in Figure 6.1. The model used does not take into account such edge effects. Since few of the largest particles will be entirely inside the beam most of these particles will not contribute to the SAXS signal the way the model predicts, and the average particle diameter will seem smaller when fitting the experimental data to the theoretical model.

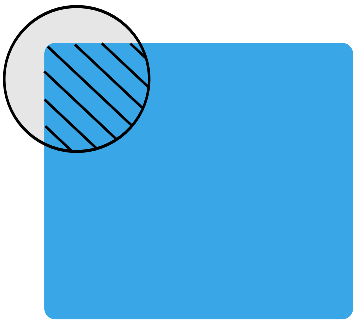

Figure 6.1: An example of a partly illuminated talc particle. Only parts of the gray talc particle is inside the X-ray beam, indicated with a blue square. Because the X-ray beam does not see the entire particle, only the marked portion of the particle inside the beam will create scattering in the SAXS regime.

Another important remark regarding the model used for fitting the SAXS signal is the lack of structure factor. It has not been seen any significant ordering between the particles in the experimental data. By including a structure factor in the SAXS signal, additional Bragg peaks should appear. The SAXS signal is falling off monotonically, and the experimental scattering fits rather well when fitting it to the form factor of a spheroid. This should imply no significant contribution from a structure factor. The reason why the structure factor is not significant, is most likely the fact that the dimensions of the particles are so large compared to the X-ray beam that the scattering from the different particles are not scattering coherently. The intensity will then add linearly, without interference from how the particles are structured compared to each other.

In the theory chapter, a model for handling scattering from polydisperse particles was presented. This model consists of a weighted sum of the form factors for the differently sized particles. Because of the large size of the particles, the oscillation frequency of the Bessel function in Equation 3.21 and 3.22 will be large in q-space. To prevent under-sampling the form factor, a large number of q-values have to be used in the calculation to get the correct shape of the form factor. Because of this it could take several days to calculate the form factors for the different oriented particles for all angles in a tomography scan. Since calculating the form factors for only single sized particles in a tomography scan could take several days, calculating form factors for several differently sized particles, and then taking a weighted sum of them, would take too much time. At the early stage it was uncertain how well the method would work and therefore spending a lot of time on something that perhaps would be unnecessary seemed unwise. Now that the method has proven to work it can be relevant to use the model for polydispersity as presented. Instead of the model presented, a much easier method was used, where the theoretical data was smoothed by a Gaussian function, accounting for both polydispersity and finite detector resolution. The crude convolution with a Gaussian function to fit the theoretical data with the experimental data was successful and therefore viewed as sufficient for the method used in this thesis. By applying the model for polydispersity presented in the theory, additional information could perhaps be drawn from the system. The distribution of the particle size could possibly give information on why the average particle size is as it is seen in this thesis, but this was not seen as a significant goal of this thesis, and therefore postponed for later work.

6.3 Reconstructing Orientation Distribution

6.3.1 Reconstruction Based on Simulated Annealing

When reconstructing the orientation distribution by Simulated Annealing, as seen in Figure 5.8, the orientation distribution has little resemblance to the true orientation distribution seen in Figure 2.4. The fact that four of the cases with different initial conditions turned out to give the exact same results, can imply that the T and δT values are not good enough tuned to give a converging solution. Even in the single case where the final orientation distribution was different from the other cases, the difference was only marginal. The reason why these are almost exactly the same comes most likely from how the routine was implemented in `Matlab`. To get random numbers the *rand* function in `Matlab` was used. This is basically just a list of random numbers which is the same each time `Matlab` is opened. For this reason every simulation would use the same random numbers. This means that during each Monte Carlo step, the same voxel would be tried updated to the same new value, and the only difference would come when it should check according to the probability distribution if the change was allowed to take place. The problem is not the pseudo random function implemented in `Matlab`, but that the initial T and δT were too similar between the different configurations compared to the initial value of the energy. These values decides what step are allowed to take place and how quick it should settle for the closest minimum. Finding better values for T and δT is crucial for making this method work.

It could also be theorized that the final distribution found indeed is a local minimum. The behavior of the energy as function of number of iterations should be investigated to see if where it settles looks like a local minimum, or if the energy is roughly the same for all iterations.

The reason why this approach was not explored further, and tried to make improvements on the model, is due to the fact that the preliminary results showed very little resemblance with the true distribution, even though the initial guess of the distribution was fairly close to the true distribution. If this method would be used on real experimental data, where the initial orientation is totally unknown, it would be even harder to get this method to work. Another reason for not going further with this method is that it is very time consuming. In this idealized case where the form factor is precisely known it looks like the algorithm would need considerably more iterations before finding the optimal solution. The number of iterations used in this simulation was 300 000 and took roughly 48 hours. Although this was without any optimization of the code, it mostly used internal `Matlab` functions which in general are well tested and optimized for speed. Even if the code could be optimized to run several times faster it is unlikely that a sufficient amount of iterations could be achieved to get close to the optimal solution. It would for the case demonstrated in this thesis be $36^{63 \cdot 151}$ different possible configurations of the iPP model, since each of the 63×151 voxels could have 36 different values. This is vastly more configurations than any computer could have time to check systematically, and the number of iterations to reach the optimal solutions by Simulated Annealing is hence also very large.

If this method is to be improved, there are some improvements that could be done. First of all the *radon* function used in `Matlab` is a big time consuming choking point. If a method for finding how far an X-ray beam travels through an area where the orientation has a specific value could be found, which is significantly faster than the implemented *radon* function in `Matlab`, then this would help to speed up the process. If the function which is to be minimized had an extra term which was high if the gradient of the orientation distribution was high, this could remove most of the $36^{63 \cdot 151}$ possible configurations which the orientation distribution is allowed to have. This is because a high gradient in the orientation distribution would mean that neighboring voxels have a large difference in orientation, and this is something that is unlikely for many cases, including the test sample used here. There are a lot more configurations with a high gradient in the orientation distribution than with low gradient, therefore only a few configurations are allowed. Checking the gradient will however slow down the process, and to check how much the gradient should influence the system would also need some fine tuning. Another alteration which could be made, would be lowering the number of possible orientations the talc particles inside the sample could have. It was used 36 different orientations which in retrospect is obviously too high. Combining voxels to regions, meaning that changing one voxel would change the entire region it is part of, would probably be an improvement. Since it is known that the orientation varies slowly, it is probably not necessary to have the possibility to change each voxel independently, thus speeding up the algorithm since it will change more voxels in less time.

A big disadvantage with the formulation of this problem is the lack of knowledge about how the energy function used behaves and how the the global minimum is. For instance, if the energy function is almost equal for all configurations, except at a very steep drop close to the global minimum, it will be very difficult to find this point in configuration space.

The suggestions for improvements presented here could very well help getting closer to the correct orientation distribution. However, since the initial test of retrieving the orientation distribution from simulated scattering, with no polydispersity and no noise, failed, it was decided to focus on retrieving the orientation distribution based on a linear set of equation, since this method showed much more promise.

6.3.2 Reconstruction Based on a Linear Set of Equations

Reconstruction from Simulated Perfect Data

Figure 5.9 shows excellent agreement between the true orientation distribution in the model of the iPP sample, and the retrieval of the orientation distribution based on the simulated horizontal scattering signal. Figure 5.9 (b) was reconstructed based on the method outlined in Section 3.8.1. We have thus proven it possible to reconstruct the orientation in a sample based on the horizontal scattering pattern, if it is a priori known that one of the axis of symmetry always is pointing along the rotation axis of the tomography scan.

Our method is however limited by some assumptions. The precise form factor has to be known for all different orientations. It is therefore required that the theoretical model for the scattering is in very good agreement with the experimental data. The method is also based on the assumption that the scattering intensity from each different orientation region adds linearly and is proportional to the distance it travels through the given region. In addition the system has to consist of a single type of particles, with no polydispersity, no noise and high detector resolution. Under ideal conditions it is thus possible to retrieve the orientation distribution of the talc particles in the sample.

The biggest disadvantage with this method comes from the symmetry of the particles being imaged. By Friedel's law, the form factor is symmetric around the origin, e.g. $|F(\mathbf{q})|^2 = |F(-\mathbf{q})|^2$. Every scattering pattern in the horizontal direction can come from particles with two different orientations. This is demonstrated in Figure 6.2. Here it is seen that the scattering patterns, outlined by the green ellipses, from two differently oriented particles have the exact same intensity value for the scattering vector $\mathbf{q}$ in the horizontal plane. Because of this problem, it is not possible to reconstruct every single orientation in the sample. This would lead to a singular scattering

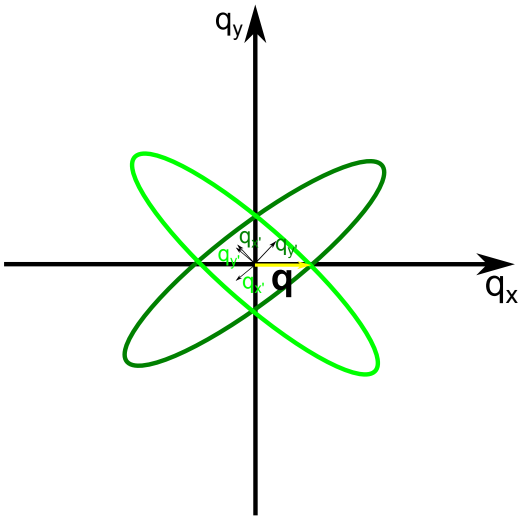

Figure 6.2: The scattering patterns from two differently oriented particles are outlined by the green ellipses. The intensity for the scattering vector **q** is identical for both scattering patterns, and it is therefore impossible to distinguish these particles by only looking at the scattering in the horizontal direction.

matrix S, because two or more horizontal scattering intensities would be the same between different oriented particles. In practice, discrete set of orientation intervals is made, where the initial particle orientation is denoted by ϕ_m in interval number m. This set of orientations is chosen in such a way that the theoretical horizontal scattering intensity is not equal for any two orientations in any angle of the tomographic scan. A possible way around this problem could be by using the entire 2D scattering pattern to separate those particles which have orientation giving the same horizontal scattering intensity. These particles will not necessarily give same intensity for other scattering vectors, as seen in Figure 6.2.

Reconstruction From Simulated Polydispersive Data

Figure 5.10 showed how the reconstruction works for simulated data when polydispersity and finite detector resolution is taken into account. Everything else is done under "ideal" conditions, meaning that only talc particles scatter, and it is no noise or background radiation in the detector signal. The scattering signal is also proportional to the form factor squared and to each different orientation region the X-ray beam travels through, and adding linearly to give the full signal. Even with conditions as ideal as this the reconstruction algorithm has problems with recreating the orientation distribution of 36 regions with different orientation, because many of the line artifacts are shadowing the details of the orientation distribution. Many of these artifacts could possibly be removed by setting various thresholds and forcing continuous and slow variation of the orientation gradient. This means however that it is necessary with pre-known knowledge of the sample.

Even under nearly perfect conditions, the reconstruction algorithm has problems retrieving the orientation distribution. It was not chosen to try to optimize the reconstruction of the simulated data with polydispersity and finite detector resolution taken into account, because even though there are many line artifacts in the tomogram, the different regions are clearly visible. It was also believed that 36 different regions would give a much higher resolution than what it could be expect to retrieve from the experimental data. It demonstrates that the method used for retrieving the orientation distribution has a practical upper limit when dealing with polydispersive particles.

Reconstruction From Experimental Data

Figure 5.12, 5.13 and 5.14 show how the orientation distribution of the talc particles is when two-, four- and six-modal orientation distribution are attempted reconstructed from the experimental data. It is clear that the main features of the talc particles orientation distribution are retrieved. This is seen by noting that the red area is located at the correct place for all the reconstructions, as well as that the area along the short sides have "light blue" orientation.

When looking at the tomogram where four different orientations are reconstructed, it is apparent that the "light blue" region is not so dominant, as it was for the bimodal orientation. This is to be expected since in the bimodal orientation distribution the "light blue" region represented the angle interval $\phi = \langle -45, 45]$ while in the 4-modal it only represents $\phi = \langle -22.5, 22.5]$. Here the "green" and "purple" orientations are placed between the "light blue" and "red" orientation, as it should. The "green" and "purple orientations" are also found in the correct direction, from bottom left to top right and top left to bottom right. The "light blue" orientation is placed mainly along the short edges in the sample and in the center, as it should be. Another apparent feature is the fact that the regions of "red" orientation are almost joined together close to the center, which agrees well with the true orientation distribution. This was not seen in the tomogram reconstructed with only two different orientations. The resolution of the tomogram has clearly gone up by going from two to four reconstructed orientations, since it is possible to distinguish more distinct features.

The cost of separating characteristic features is many more artifacts. There is no distinct border between the different orientation regions. Larger parts of the interior also have no assigned orientation. This is likely caused by the fact that the theoretical model of the scattering does not agree perfectly with the experimental data. The calculated distances the X-ray beam travels through each orientation region, $\{a_{\phi_i,x,\psi}\}$, are not consistent between different angles ψ. The integrated value along each projection angle should be the same for each angle in the tomography scan according to theory. This would just be the area of the function f_m, which is independent of the coordinate system used, which means independent of rotation angle ψ. The inconsistencies in the sinogram, in Figure 5.11, can be seen by looking at the projections when the projection angle $\psi = 63°$. Here, the sinogram shows that the X-ray beam does not travel through the region with the given orientation for any projections. It is obvious that this is impossible, since this would imply that this region does not exist, as it clearly does because it is present for most of the other ψ-angles. This is causing many of the streak artifacts and regions with no orientation inside the sample.

Another observation is the fact that the "purple" and "green" orientation is more scattered than the "red" and "light blue orientation". Scattered means in this case that the regions are not continuous and connected. The "purple" and "green orientation" represents talc particles with median orientation $\phi = -45°$ and $\phi = 45°$, respectively. By comparing with the true orientation distribution it is noted that the regions with talc particles with this orientation are very thin for most projections, while the regions with "red" and "light blue orientation" are thicker. Thin and thick refer to the distance, $a_{\phi_i,x,\psi}$, the X-ray beam travels through the region for a single projection. The reconstruction algorithm seems to have problems reconstructing regions in the sample which are thin for most projections.

Trying to reconstruct regions with six different possible orientations, gives the main features for the "red" and "light blue orientation" in the same way as for the tomogram trying to recreate four regions. The tomogram where six regions are reconstructed is however suffering from more artifacts. Although it is still possible to recognize the main features, the tomogram is too unclear to give any reliable insight. The orientation regions beside the "red" and "ligh blue" are more mixed into each other than for the other tomograms. It would for instance be unwise to state that a single voxel has talc particles with the direction given by the color, since the domains are scattered around, and many areas have white domains, meaning the reconstruction algorithm has not given them any specific orientation. There are mainly two reasons why this tomogram fails as much as it does in retrieving the orientation distribution. First, since the scattering intensity from polydispersive particles is varying slowly it is difficult to separate particles of almost the same orientation. This can be seen, as part of where the orientation should be "red" is now "pink". These two orientations have almost the same form factor, and are therefore difficult to separate when fitting the data. Second, the 2D scattering patterns were packed to reduce the storage space, and speed up calculations. Figure 4.3 shows how the scattering pattern on the detector was divided into 16 different regions. Because of this sectioning, regions 1, 8, 9 and 16 had to be used for the horizontal scattering signal, since they were all equivalent. Since region (8 and 9) and (1 and 16) form an angle of 45°, this is the best possible resolution which can be achieved when trying to retrieve the orientation distribution. It would for example be impossible to separate two talc particles with 10° separation in orientation because scattering in the $q_{y'}$ direction of the internal coordinate system of each particle would both be scattered to the same sector on the detector, where it is measured to be $\mathbf{q}$ according to the laboratory frame. This is visualized in Figure 6.3.

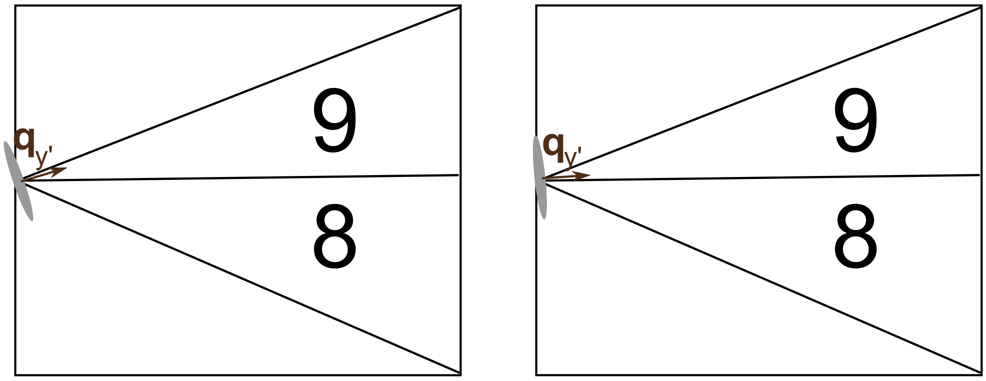

Figure 6.3: The figure demonstrates the resolution limit in retrieving the orientation distribution of the talc particles. Two differently oriented talc particles will both have their $q_{y'}$-direction scatter into sectors 8 and 9, which means that due to how the data are stored it will be marked as both particles are scattering into the horizontal plane and are therefore have the same orientation.

To get around this problem, the entire detector signal could be used. This will increase the theoretical maximal resolution in the orientation distribution to 22.5° because it is then possible to separate scattering into each sector. To increase it further, the raw data picture would have to be processed again, increasing the number of sections the detector is divided into. By doing this, it would be unnecessary to use the entire 2D scattering pattern, since narrowing the angle forming the horizontal scattering also will increase the maximum theoretical resolution. A problem with this will be lowering the counting statistics, making it necessary to increase the exposure time when performing the experiments.

6.4 Further work

There are a number of suggestion for improving the reconstruction algorithm. The fact that the method of retrieving the orientation distribution by a linear set of equations works rather well for a few angle intervals shows that the method is promising. It is thought that improving the talc scattering model will further improve the results. If the entire scattering pattern on the detector is used then additional constraints are applied to the problem. The scattering should not only fit for in the horizontal direction, but also for the vertical and along a diagonal on the detector. It is then visualized that a numerical algorithm can work with the data retrieved and improve it further. By applying constraints, as continuous domains, slow variation in the orientation distribution and that the sinogram shall be consistent between every angle ψ, then an iterative algorithm can improve the result further. One numerical algorithm which could fit this problem is the Simulated Annealing method presented in this thesis, but also other algorithms are possible.

The reason why the Simulated Annealing method did not work in retrieving the orientation distribution was because it tried to recreate the scattering patterns by altering the orientation in each voxel. This was both time consuming and very large problem with many variables. By minimizing a function which already uses the fitted scattering pattern it is believed that the method will work better and faster.

Chapter 7

Conclusion

Two different methods, for retrieving the orientation distribution of talc particles in a sample of isotactic polypropylene, have been presented in this thesis. The first method used a numerical approach of Simulated Annealing and the second method used a linear set of equations to find the distances the X-ray beam traveled through the different oriented regions for each projection.

7.1 Retrieving Orientation Distribution By Simulated Annealing

As seen in Figure 5.8, Simulated Annealing shows little promise in retrieving the orientation distribution of the talc particles inside the sample. Although several alterations can be made to improve the algorithm, as discussed in Section 6.3.1, it is seen as unlikely that these would improve it considerably. The results of this method to retrieve the orientation distribution is added to this thesis to discourage future work on trying to retrieve the orientation distribution from the SAXS pattern by Simulated Annealing in the same way as presented in this thesis. If however this method is decided to be used, then it is advised to note the suggestions for improvements discussed, and use it on a problem formulated after the orientation distribution has been retrieved by a linear set of equations, and thus improve that result.

7.2 Retrieving Orientation Distribution By Linear Set of Equations

It can be seen from Figure 5.12 and 5.13 that the main features of the true orientation distribution of the talc particles have been retrieved. The tomograms suffer from many artifacts, with regions marked with orientation outside the sample, regions inside the sample with no specified orientation, non-continuous domains and unsharp borders between regions with different orientation. Despite this, the method shows promise, and with further improvements the accuracy of the position of the regions could be improved. From an academic standpoint it is very interesting with further work on this project, since earlier work in SAXS tomography have only focused on the vertical scattering or assumed spherical particles.

It can also be seen from Figure 5.14 that when trying to retrieve the orientation distribution with higher resolution than the detector segmentation allows, the retrieved orientation regions would be mixed up in each other. Unfortunately, this segmentation has also hindered the progress in determining how many regions which can be retrieved and still have the main features visible as in the true orientation distribution. It is not certain wether this method with these data will or will not be able to resolve six different regions. It does, however, seem to work rather well for four regions.

As noticed earlier, the tomograms are far from perfect, and the different orientation regions are not precisely placed inside the sample. This makes it at the current moment difficult to use our method for *in situ* studies of mechanical testing of the iPP samples, which was one of the desired goals for this thesis. To notice differences, with the current method, in the orientation of the talc particles after the sample has been modified in some way, very large changes in the orientation distribution would be needed. These changes in the orientation distribution are probably larger than what would be possible without destroying the sample.

It has been demonstrated that polydispersity makes it difficult to retrieve the orientation distribution because the scattering signal is smoothed out, making the form factor of two slightly differently oriented talc particles almost identical. How symmetry in the scattering prohibits a continuous orientation distribution to be retrieved is also shown. To improve the resolution and accuracy of the method further, work should be put into the model of how the talc particles scatter and the precise attenuation coefficient of the sample should be measured. The talc particles which scatter in the sample can also be argued to be too large compared to the beam. The largest particles were approximately 10 μm in diameter, which is rather large compared to the $20 \times 20\ \mu\mathrm{m}^2$ beam size. To see how well our method works, other samples should be tested, preferably systems with smaller scatterers, with less polydispersity and with a preferred direction of orientation. By doing an experiment on such a system it can be known if the limiting factor is the model and reconstruction algorithm itself, or if it is the scattering talc particles in the iPP sample.

7.3 Summary

It has been shown that it is possible to reconstruct the spatially varying orientation distribution of particles, with a preferred orientation inside a sample, by using the method of a linear set of equations. Specifically, we have retrieved the orientation distribution of talc particles in a sample of isotactic polypropylene by using the horizontal signal in a small-angle X-ray scattering tomography scan. This method and and the data in this thesis are however not yet accurate enough to give a precise localization of the different oriented regions inside the sample, and can thus not be used for *in situ* studies at the present moment. It is however believed that with further work this can be achieved.

The method presented is not specialized for talc particles, and it should be possible with minor alterations to use it on other systems. If it is known that the particles involved have a preferred direction of orientation then the only part needed to be changed would be the form factor of the particle.

Bibliography

[1] A. C. Kak and M. Slaney, *Principles of Computerized Tomographic Imaging.* Society for Industrial and Applied Mathematics, 2001.

[2] T. H. Jensen, M. Bech, O. Bunk, M. Thomsen, A. Menzel, A. Bouchet, G. L. Duc, R. Feidenhans'l, and F. Pfeiffer, "Brain tumor imaging using small-angle x-ray scattering tomography," *Physics in Medicine and Biology*, vol. 56, no. 6, pp. 1717–1726, 2011. Available online.

[3] T. Jensen, M. Bech, O. Bunk, A. Menzel, A. Bouchet, G. L. Duc, R. Feidenhans'l, and F. Pfeiffer, "Molecular X-ray computed tomography of myelin in a rat brain," *NeuroImage*, vol. 57, no. 1, pp. 124–129, 2011. Available online.

[4] C. G. Schroer, M. Kuhlmann, S. V. Roth, R. Gehrke, and N. Stribeck, "Mapping the local nanostructure inside a specimen by tomographic small-angle x-ray scattering," *Applied Physics Letters*, vol. 88, no. 16, 2006. Available online.

[5] H. Granlund, J. B. Fløystad, M. Esmaeili, E. T. Bakken, M. Bech, P. E. Vullum, E. Andreassen, and D. W. Breiby, "Mapping structural gradients in isotactic polypropylene using scanning wide-angle x-ray scattering," *Polymer*, vol. 54, no. 7, pp. 1867 – 1875, 2013. Available Online.

[6] M. Esmaeili, J. B. Fløystad, A. Diaz, K. Høydalsvik, M. Guizar-Scairos, J. W. Andreasen, and D. W. Breiby, "Ptychographic X-ray Tomography of Silk Fiber Hydration," *Macromolecules*, vol. 46, no. 2, pp. 434–439, 2013. Available online.

[7] R. Kongsmo, "Prosjektrapport," Master's thesis, Norwegian University of Science and Technology, 2012.

[8] E. T. Bakken, "Wide and Small Angle X-ray Scattering on Talc Filled Polypropylene," Master's thesis, Norwegian University of Science and Technology, 2013.

[9] P. J. T. Morris, *Polymer Pioneers: A Popular History of the Science and Technology of Large Molecules.* Chemical Heritage Foundation, 2005.

[10] C. M. I. Consulting, "Market study: Polypropylene," 2012. Available online.

[11] F. P. van der Burgt, *Crystallization of isotactic polypropylene The influence of stereo-defects.* PhD thesis, Technische Universiteit Eindhoven, 2002. ISBN 90-386-2674-6.

[12] M. A. G. C. Marco, G. Ellis and J. M. Arribas, "Analysis of the dynamic crystallisation of isotactic polypropylene/α-nucleating agent system by dsc," *Thermal Analysis and Calorimetry*, vol. 68, pp. 61–74, 2002. Available online.

[13] S. Z. D. Cheng, J. J. Janimak, and J. Rodriguez, "Crystalline structures of polypropylene homo- and copolymers," *Polypropylene: Structure, blends and composites*, vol. 1, pp. 31–52, 1995. Available online.

[14] F. Khoury, "The spherulitic crystallization of isotactic polypropylene from solution: On the evolution of monoclinic spherulites from dendritic chain-folded crystal precursors1," *Journal of Research of the National Bureau of Standards -A Physics and Chemistry*, vol. 70A, no. 1, 1966. Available online.

[15] Y. Wang, C. Chen, J.-Z. Xu, J. Lei, Y. Mao, Z.-M. Li, and B. S. Hsiao, "Suppressing of γ-crystal formation in metallocene-based isotactic polypropylene during isothermal crystallization under shear flow," *The Journal of Physical Chemistry B*, vol. 116, no. 16, pp. 5056–5063, 2012. Available online.

[16] B. L. Henke, E. M. Gullikson, and J. C. Davis, "X-ray interaction: Photoabsorption, scattering, transmission, and reflection at e=50-30,000 ev, z=1-92," *Atomic Data and Nuclear Data Tables*, vol. 54, no. 2, pp. 181–342, 1993. Available online.

[17] R. H. Todd, D. K. Allen, and L. Alting, *Manufacturing Processes Reference Guide.* Industrial Press Inc, first ed., 1994.

[18] R. A. Phillips and M. D. Wolkowicz, *Polypropylene Handbook.* Hanser, 2005.

[19] B. E. A. Saleh and M. C. Teich, *Fundamentals of photonics.* Wiley, second ed., 2007.

[20] D. J. Griffiths, *Introduction to electrodynamics.* Pearson, third ed., 2008.

[21] J. Als-Nilsen and D. McMorrow, *Elements of modern x-ray physics.* Wiley, second ed., 2010.

[22] C. Kittel, *Introduction to Solid State Physics.* Wiley, eighth ed., 2005.

[23] J. Daillant, *X-ray and Neutron Reflectivity: Principles and Applications.* Springer, first ed., 2009.

[24] W. H. Press, S. A. Teukolsky, W. T. Vetterling, and B. P. Flannery, *Numerical Recipes: The Art of Scientific Computing.* Cambridge University Press, third ed., 2007.

[25] J. Nocedal and Stephen J. Wright, *Numerical Optimization.* Springer, second ed., 2006.

[26] K. G. Murty, *Linear complementarity, linear and nonlinear programming.* Heldermann, first ed., 1988.

Appendices

Appendix A

Sinograms and Tomograms from Experimental Data

The reconstructed sinograms of the distances an X-ray beam travels through a given orientation in the sample, along with the reconstructed tomogram, will be given here. The sinograms should ideally be radon transforms of the function given in Equation 3.54. All the figures are built up the same way, with the sinogram on the left, where the color indicates the distance the X-ray beam travels through an oriented area in cm. The right are the tomograms. These should ideally have the value 1 in voxels where the orientation of the talc particles is equal to the given orientation and 0 where it is not. Due to imperfect data sets a threshold was set, where all the values above 1 was set to have the given orientation. Those voxels in the sample which would succeed the threshold for multiple orientation, the voxel would be assigned the orientation from the tomogram where the value was highest. The reason why the tomograms have zero value along the vertical edges is due to zero padding in `Matlab` when the tomogram was rotated to a horizontal position.

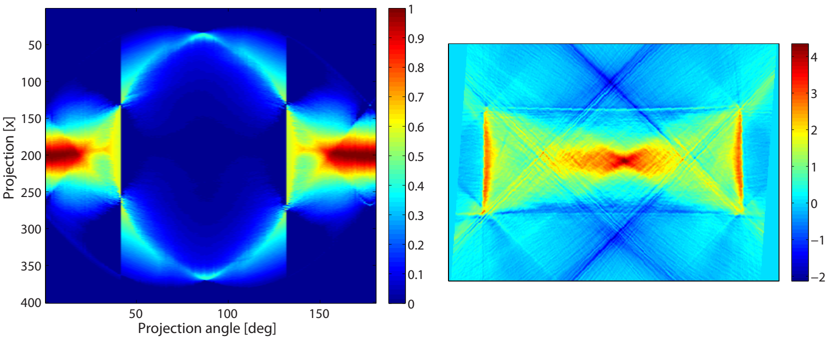

Figure A.1: 2-modal orientation distribution reconstructed. Represents orientation distribution where $\phi(s,t) = 0°$

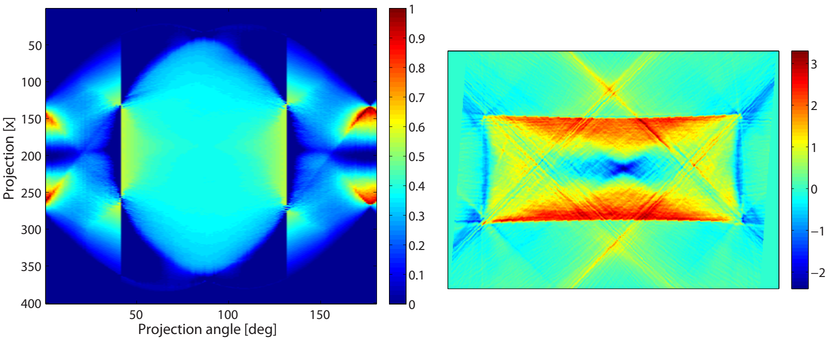

Figure A.2: 2-modal orientation distribution reconstructed. Represents orientation distribution where $\phi(s,t) = 90°$

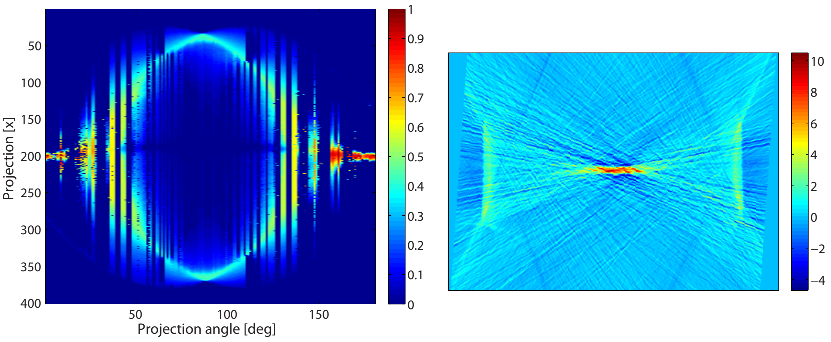

Figure A.3: 4-modal orientation distribution reconstructed. Represents orientation distribution where $\phi(s,t) = 0°$

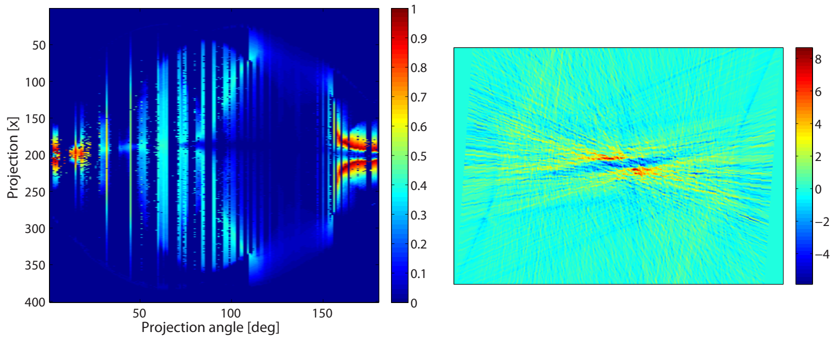

Figure A.4: 4-modal orientation distribution reconstructed. Represents orientation distribution where $\phi(s,t) = -45°$

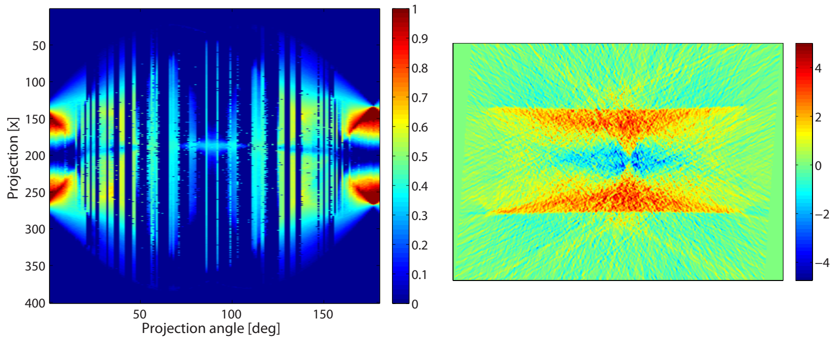

Figure A.5: 4-modal orientation distribution reconstructed. Represents orientation distribution where $\phi(s,t) = 90°$

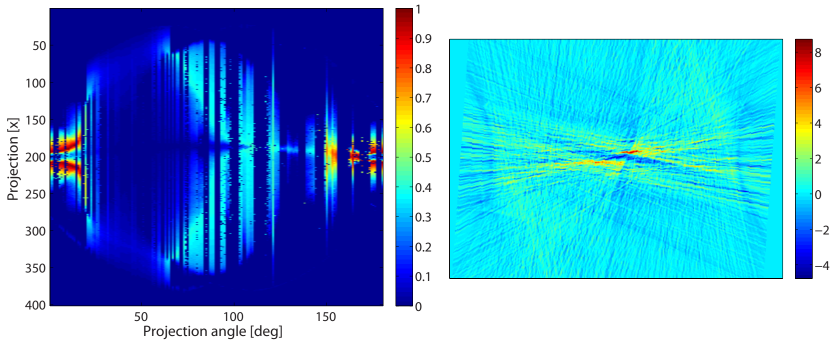

Figure A.6: 4-modal orientation distribution reconstructed. Represents orientation distribution where $\phi(s,t) = 45°$

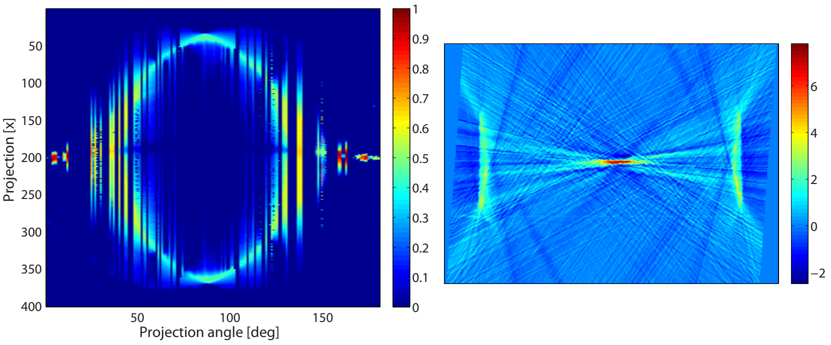

Figure A.7: 6-modal orientation distribution reconstructed. Represents orientation distribution where $\phi(s,t) = 0°$

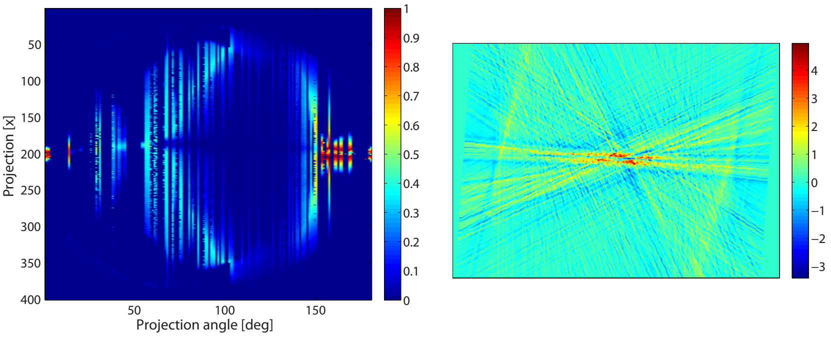

Figure A.8: 6-modal orientation distribution reconstructed. Represents orientation distribution where $\phi(s,t) = -30°$

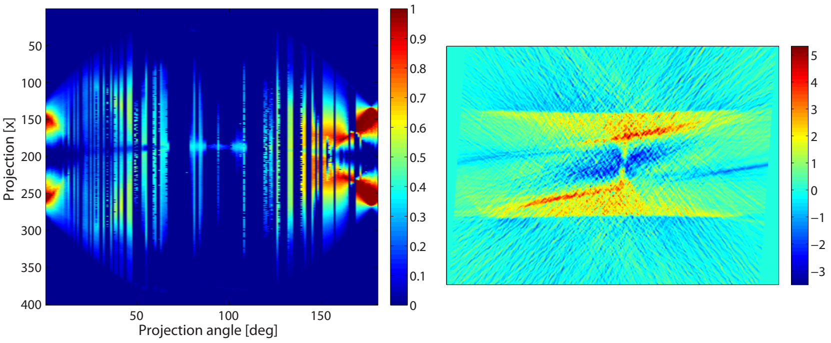

Figure A.9: 6-modal orientation distribution reconstructed. Represents orientation distribution where $\phi(s,t) = 90°$

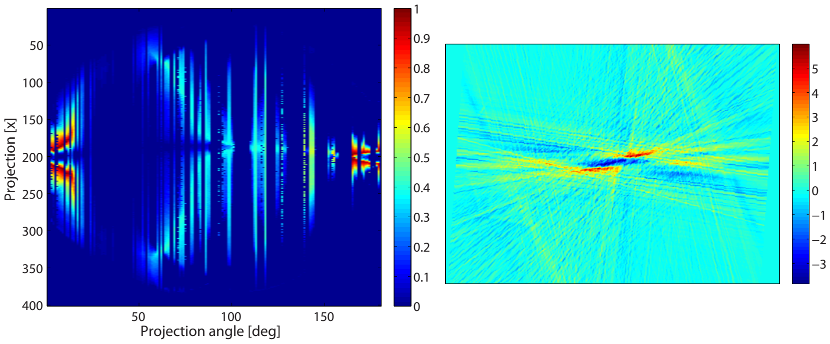

Figure A.10: 6-modal orientation distribution reconstructed. Represents orientation distribution where $\phi(s,t) = 60^\circ$

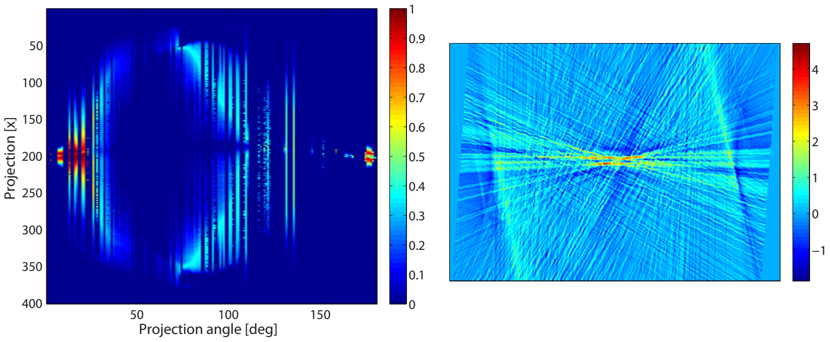

Figure A.11: 6-modal orientation distribution reconstructed. Represents orientation distribution where $\phi(s,t) = 30^\circ$

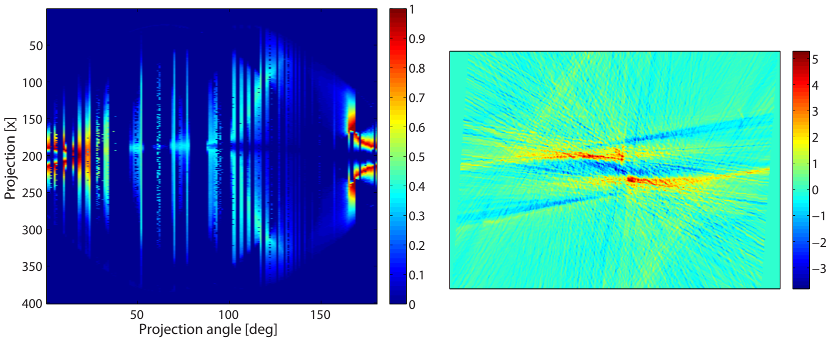

Figure A.12: 6-modal orientation distribution reconstructed. Represents orientation distribution where $\phi(s,t) = -60^\circ$

Appendix B

Poster Presented at ICXOM

A poster containing the major results from this thesis was presented at the 22nd International Conference of X-ray Optics and Microscopy (ICXOM) in Hamburg in the start of September 2013. This has been attached as an appendix to give potential readers a short and compact summary of the project. This poster does not discuss the major challenges and assumptions, but is meant to intrigue the reader to discover more about the subject.

Towards orientation distribution mapping in isotactic polypropylene by SAXS-tomography

Eirik T. B. Skjønsfjell[1], Håvard Granlund[1], Jostein B. Fløystad[1], Kristin Høydalsvik[1], Ana Diaz[2], Erik Andreassen[3], Dag W. Breiby[1*]
[1]Department of Physics, Norwegian University of Science and Technology, Norway
[2]Swiss Light Source, Paul Scherrer Institut, Switzerland
[3]Sintef Materials and Chemistry, Norway

NTNU – Trondheim
Norwegian University of
Science and Technology

The orientation distribution of talc particles in injection-molded isotactic polypropylene (iPP) has been mapped by raster-scanning X-ray scattering and SAXS tomography and showed strong alignment with the outer surfaces [1,2].

Isotactic polypropylene is a common polymer used in a vast variety of items. Raster-scanning X-ray scattering has become possible in recent years due to the improvements in detector technology, and developing methods for SAXS tomography would be of huge significance. SAXS tomography would make it possible to map *in 3D* the orientation distribution without physically destroying the sample, opening for *in situ* studies of material reorganization during mechanical loading.

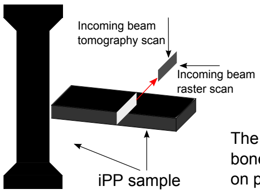

The iPP sample studied was shaped as a dog-bone, and the measurements were performed on part of the dog-bone neck.

RASTER-SCANNING

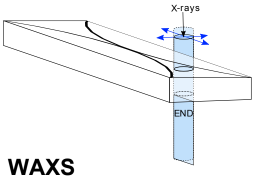

The X-ray beam was scanned over a physically cut cross section of the iPP sample. The recorded WAXS and SAXS signal gave the orientation distribution of the talc particles directly. The blue arrows indicate the directions the X-ray beam was moved during the raster-scan.

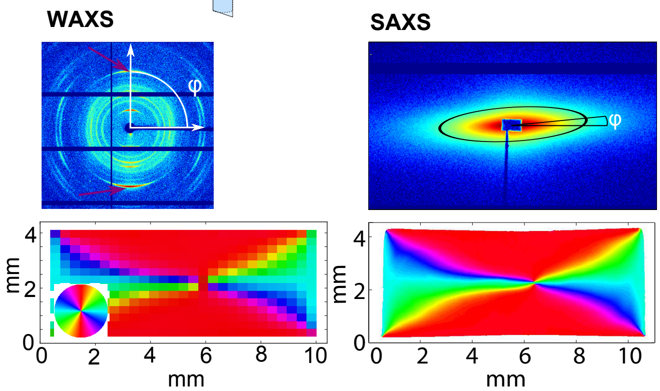

The purple arrows in the WAXS scattering pattern indicate the 006-reflection of talc. The angle φ of this reflection is mapped in the bottom left plot. The color indicates the direction of the talc *c*-axis as given by the color wheel inset. In the SAXS measurements the tilt, φ, of the ellipse (marked with the black ellipse) was measured across the iPP sample, and the resulting orientation map is shown in the bottom right figure.

Raster scans of a sample of isotactic polypropylene containing microscopic talc particles were performed, and the wide and small angle X-ray scattering patterns were recorded. The SAXS and WAXS data are in perfect agreement, as the talc *c*-axis is parallel to the talc particles surface normal.

[1] H. Granlund et al. Polymer, **54**, 1867-1875 (2013)

[2] E. Ferrage et al., Journal of Materials Science, **37**,1561-1573 (2002)

*dag.breiby@ntnu.no

SAXS TOMOGRAPHY

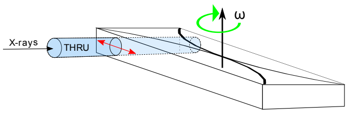

In the tomographic scan the sample was rotated around the given axis. The red arrows indicate the direction the X-ray beam was scanned for each rotation step, ω, symbolized by the green arrow.

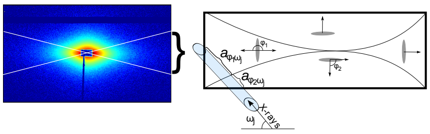

The 2D scattering pattern from an X-ray beam which travels a distance $a_{\varphi_i\omega_j}$ through several regions where the talc particles (gray disks) have different orientations. The area between the white lines represents the "horizontal" scattering used in the reconstruction of the orientation distribution.

The talc particles in the sample were approximated to be oblate spheroids with their surface normals as indicated by the figure above. The scattering intensity was assumed to be a sum were each term was proportional to the distance $a_{\varphi_i\omega_j}$ the beam travels through the region with scattering intensity equal to $I_{\varphi_i\omega_j}$. $I_{\varphi_i\omega_j}$ is proportional to the form factor of a particle with orientation φ_i. The measured scattering patterns were fitted to a theoretical scattering pattern, giving all the coefficients $a_{\varphi_i\omega_j}$, as indicated by the equations below. These radontransforms, each set of $a_{\varphi_i\omega_j}$, can then be reconstructed by ordinary reconstruction algorithms to give the orientation distribution.

$$\begin{gathered} I_{\omega_1}(Q)=a_{\varphi_1\omega_1} I_{\varphi_1\omega_1}(Q)+a_{\varphi_2\omega_1} I_{\varphi_2\omega_1}(Q)+\ldots+a_{\varphi_n\omega_1} I_{\varphi_n\omega_1}(Q) \\ \vdots \\ I_{\omega_k}(Q)=a_{\varphi_1\omega_k} I_{\varphi_1\omega_k}(Q)+a_{\varphi_2\omega_k} I_{\varphi_2\omega_k}(Q)+\ldots+a_{\varphi_n\omega_k} I_{\varphi_n\omega_k}(Q) \end{gathered}$$

$$I_{\omega_j}(Q) = S_{\omega_j} \cdot A_{\omega_j}, \qquad \begin{aligned} S_{\omega_j} &= \{I_{\varphi_i\omega_j}(Q)\} \\ A_{\omega_j} &= \{a_{\varphi_i\omega_j}\} \end{aligned}$$

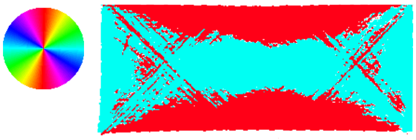

Reconstructed orientation distribution for the talc particles by SAXS tomography, using a model with only two (orthogonal) disk orientations. The directions of the talc flakes surface normal are given by the color wheel. It is noticed that the main features of the tomographically reconstructed distribution are qualitatively equal to the distribution measured by raster scanning.

Conclusion

A bimodal orientation model has quite succesfully been reconstructed by using the horizontal SAXS-signal. The main features in the tomographic reconstruction agree well with the corresponding raster-scan maps obtained on a physically cut sample. Trying to reconstruct more regions creates more artefacts in the tomogram as it becomes more difficult to retrieve the a_{φ_i}. This is because the form factor of different oriented particles will be almost similar when the angle between them is small, causing the matrix S to be close to singular. Future work will address resolving models with higher angular resolution by applying additional constraints of non-negativity, approximate symmetries and slowly varying spatial changes.